Journal of Rock Mechanics and Geotechnical Engineering 14 (2022) 2034–2057

Contents lists available at ScienceDirect

Journal of Rock Mechanics and Geotechnical Engineering

journal homepage: www.jrmge.cn

Review

A state-of-the-art review of mechanical characteristics and cracking processes of pre-cracked rocks under quasi-static compression

Liwang Liu [a,b], Haibo Li [a,b], Xiaofeng Li [a,*]

[a] State Key Laboratory of Geomechanics and Geotechnical Engineering, Institute of Rock and Soil Mechanics, Chinese Academy of Sciences, Wuhan, 430071, China
[b] University of Chinese Academy of Sciences, Beijing, 100049, China

ARTICLE INFO

Article history:
Received 12 October 2021
Received in revised form
16 January 2022
Accepted 15 March 2022
Available online 20 May 2022

Keywords:
Pre-cracked rock
Crack initiation pattern
Crack coalescence pattern
Failure pattern

ABSTRACT

The mechanical characteristics and failure behavior of rocks containing flaws or discontinuities have received wide attention in the field of rock mechanics. When external loads are applied to rock materials, stress-induced cracks would initiate and propagate from the flaws, ultimately leading to the irreversible failure of rocks. To investigate the cracking behavior and the effect of flaw geometries on the mechanical properties of rock materials, a series of samples containing one, two and multiple flaws have been widely investigated in the laboratory. In this paper, the experimental results for pre-cracked rocks under quasi-static compression were systematically reviewed. The progressive failure process of intact rocks is briefly described to reveal the background for experiments on samples with flaws. Then, the nondestructive measurement techniques utilized in experiments, such as acoustic emission (AE), X-ray computed tomography (CT), and digital image correlation (DIC), are summarized. The mechanical characteristics of rocks with different flaw geometries and under different loading conditions, including the geometry of pre-existing flaws, flaw filling condition and confining pressure, are discussed. Furthermore, the cracking process is evaluated from the perspective of crack initiation, coalescence, and failure patterns.

1. Introduction

After complicated geological diagenesis, flaws or discontinuities with different sizes and shapes are abundantly formed in rock materials, which significantly influence their mechanical behaviors and cracking processes under different testing conditions (Bobet, 2000; Lu et al., 2015; Zhao et al., 2019). According to the scale varying from several micrometers to tens of kilometers, these discontinuities can be divided into mineral cleavage, grain boundary, joint, bedding plane, fault, etc. (Fig. 1). Furthermore, different minerals, such as clay, calcite and quartz, could fill discontinuity interspace to form veins (Virgo et al., 2013; Nevitt et al., 2014, 2017). When external loading is applied to rocks, the stress concentration occurring around discontinuities would induce initiation, propagation and coalescence of microcracks, ultimately resulting in the irreversible failure of rocks (Bieniawski, 1967). In engineering practices, the existence of faults, joints and bedding planes significantly affects the stability and safety of engineering structures, such as tunnel excavation (Qiu et al., 2014), rock slope stability (Brideau et al., 2009), and mine pillar failure (Esterhuizen et al., 2011). Therefore, it is of great importance to investigate the mechanical characteristics and cracking processes of pre-cracked rocks.

To investigate the above problems in the laboratory, pre-existing flaws or discontinuities were artificially fabricated. The materials prepared for experiments include Columbia resin (Bombolakis, 1968), glass (Hoek and Franklin, 1968), polymethylmethacrylate (PMMA) (Nemat-Nasser and Horii, 1982), gypsum (Bobet and Einstein, 1998), rock-like material (Zhuang et al., 2014), and rocks (Zhou et al., 2019b). According to the discrepancy of the flaw geometry, two- (2D) and three-dimensional (3D) flaws were classified (Dyskin et al., 2003; Wong et al., 2006; Yin et al., 2014; Lu et al., 2015). The mechanical properties and deformation behaviors of pre-cracked samples were investigated in different experiments, including uniaxial compression, biaxial compression, and hydraulic fracturing tests (Shen, 1995; Wong and Einstein, 2006; Gonçalves da Silva and Einstein, 2018). Combining with monitoring measurement apparatus, the crack initiation, propagation and coalescence processes were directly observed in pre-cracked samples

* Corresponding author.
E-mail address: xfli@whrsm.ac.cn (X. Li).
Peer review under responsibility of Institute of Rock and Soil Mechanics, Chinese Academy of Sciences.

https://doi.org/10.1016/j.jrmge.2022.03.013

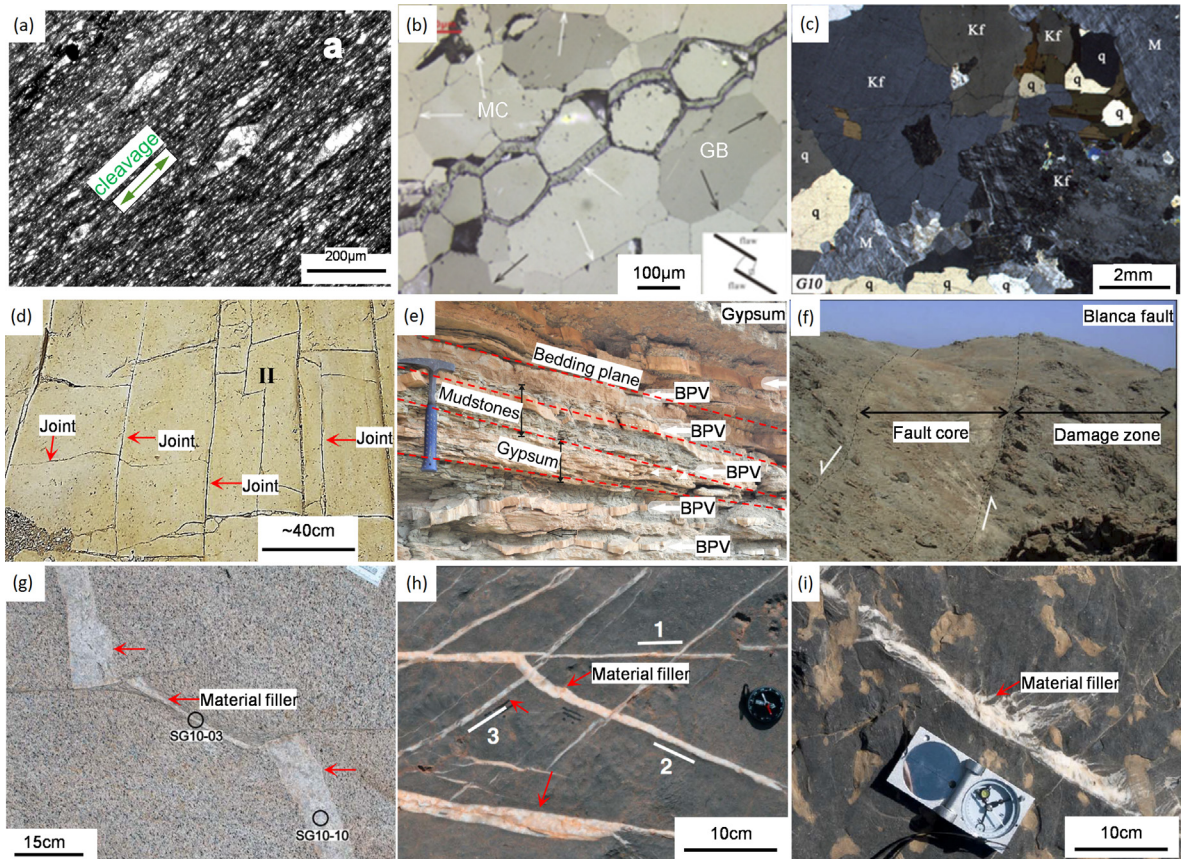

Fig. 1. Discontinuities with different scales in rock materials: (a) Penetrative cleavage from the Liskeard area, East Cornwall (Geoff Tanner, 2016); (b, c) Microcracks and grain boundaries, in which 'MC' means microcracks, 'GB' means grain boundaries, 'M' means mica, 'q' means quartz, and 'Kf' means K-feldspar (Güneş Yilmaz et al., 2011; Cheng et al., 2015); (d) Orthogonal cross joints observed in the Zhiha Formation (Levi et al., 2019); (e) Bedding planes in sedimentary rocks, in which 'BPV' means bedding plane veins (Abaab et al., 2021); (f) Field photo of the Blanca fault (Mitchell and Faulkner, 2009); and (g–i) Discontinuities filled by other materials, reproduced with permission from AGU (Nevitt et al., 2014, 2017).

containing one, two and multiple flaws (Bobet, 2000; Feng et al., 2009; Park and Bobet, 2010; Zhou et al., 2014). To our knowledge, the research scope for pre-cracked samples is relatively wide, mainly including theoretical analysis, experimental test, and numerical simulation (Horii and Nemat-Nasser, 1985; Lin et al., 2021; Liu et al., 2021a). Although numerous experiments have been conducted on pre-cracked samples, few review articles are currently available (Sarfarazi and Haeri, 2016; Wang et al., 2019b; Cao et al., 2019; Zhou et al., 2021b).

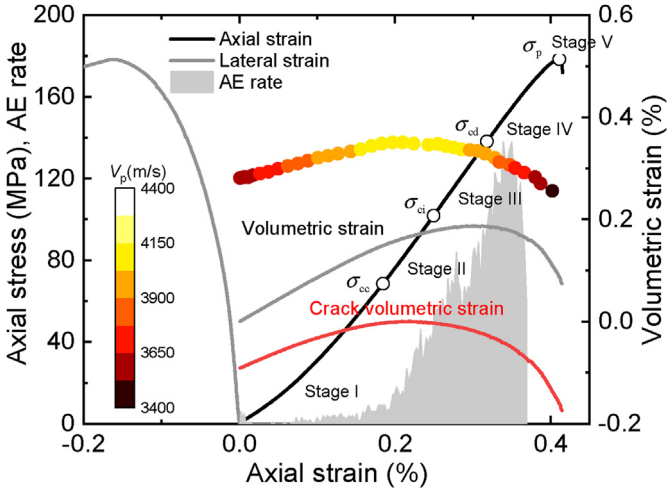

Fig. 2. Progressive deformation process of intact rocks under compression. V_p is the P-wave velocity along axial loading direction, σ_{cc} is the crack closure stress, σ_{ci} is the crack initiation stress, σ_{cd} is the crack damage stress, and σ_p is the peak stress (modified after Zhang et al., 2020).

This review aims to systematically present the results of pre-cracked rocks in compressive experiments, in which the theoretical analysis and numerical simulation are excluded. The pre-existing flaw is 2D, and the loading condition is quasi-static. The outline is organized as follows. Section 2 briefly describes the progressive deformation of intact rocks to reveal the experimental background of pre-cracked samples. Section 3 reviews the noncontact measurements used in experiments. The mechanical characteristics and crack initiation patterns of samples with one flaw are summarized in Section 4, followed by the crack coalescence of samples with two flaws in Section 5. Section 6 depicts the mechanical characteristics and failure patterns of samples with multiple flaws, and Section 7 summarizes the entire paper.

2. Brittle deformation and crack stress of intact rocks

2.1. Brittle deformation of intact rocks

Based on the axial and lateral deformation obtained by strain gages, it is found that the failure process of intact rocks under compression is related to microcrack growth and has progressive characteristics. Tal et al. (2016) utilized image processing and

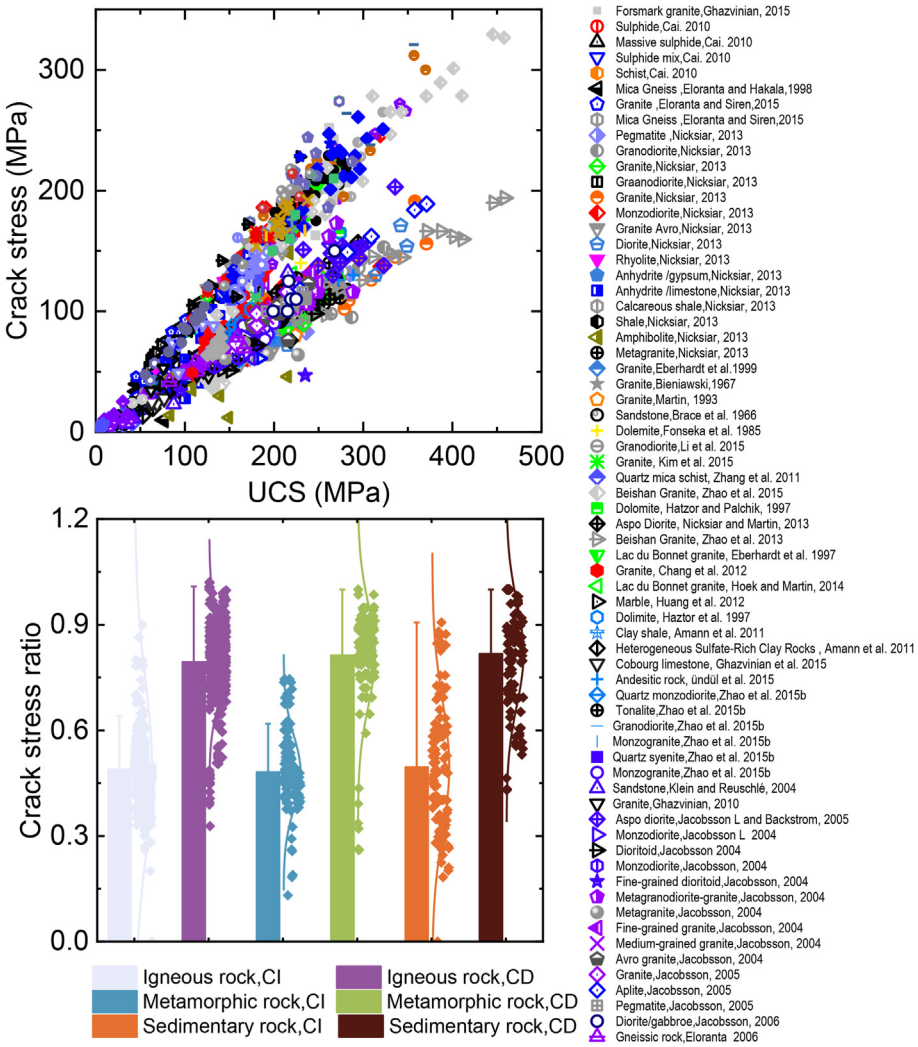

Fig. 3. The relationships between crack initiation stress (σ_{ci}), crack damage stress (σ_{cd}) and UCS for different rocks (Li et al., 2020). CI and CD are short for crack initiation and crack damage stresses, respectively.

strain-mapping techniques to directly investigate the microcrack growth, and they indicated that microcracks were formed around the grain boundary before peak stress and penetrated mineral grains after peak stress. As shown in Fig. 2, the progressive characteristics can be typically divided into the following five stages (Martin and Chandler, 1994; Xue et al., 2014). Stage I is called crack closure stage, which involves the closure process of microcracks existing inside materials, and the crack closure depends on the initial rock porosity or microcrack state. When the crack direction inclines at an angle to the compressive stress, the crack closure stage occurs (Nicksiar and Martin, 2012). After most microcracks have closed, the sample enters linear and elastic deformation at Stage II. If the compressive stress exceeds the local strength of rocks, stress-induced cracks would initiate and propagate, resulting in the stable crack growth (Stage III). As the stress further increases, the microcrack growth becomes nonlinear and rocks begin to dilate. The reverse point of volumetric strain represents the onset of unstable crack growth (Stage IV). At Stage V, the elastic energy stored in samples and loading apparatus is violently released, and thus this stage is hard to observe. In the progressive process, three crack stress levels between adjacent stages are important for understanding the microcrack growth states, i.e. the crack closure, initiation and damage stresses.

2.2. Crack closure stress

As to the onset of Stage II, the crack closure stress is related to the contraction of microcracks. The crack closure phenomenon decreases rock porosity, which results in nonlinear deformation before the axial stress exceeds the crack closure stress. From the previous study by Li et al. (2020), the ratio of crack closure stress to peak stress is not constant for different rocks. The nonlinear deformation induced by the crack closure seldom occurs for the hard rocks or sedimentary rocks with low porosity. Therefore, it is difficult to obtain a clear relationship between the crack closure stress and the peak stress.

2.3. Crack initiation stress

Crack initiation is important to characterize the initiation of irreversible damage in rocks. Brace et al. (1966) primarily indicated that the stress level for crack initiation is about 0.3–0.5 times the uniaxial compressive strength (UCS) for rocks with low porosity. Fig. 3 summarizes 953 tests to investigate the relationship between crack initiation stress, crack damage stress and UCS. The results illustrated that the ratio of crack initiation stress to UCS is 0.49 for igneous rocks, 0.48 for metamorphic rocks, and 0.5 for sedimentary

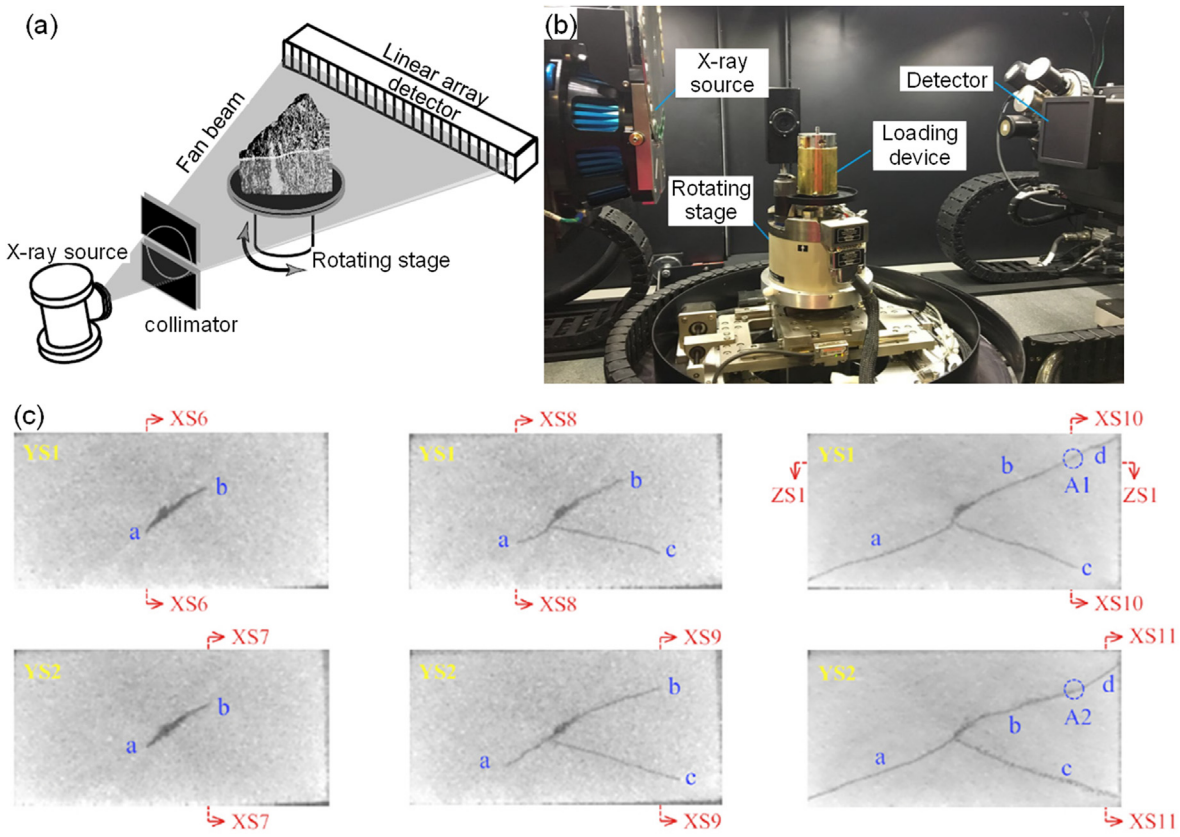

Fig. 4. X-ray CT technique and the experimental results for pre-cracked samples: (a) Schematic diagram of X-ray CT technique (Ketcham, 2005), (b) Photograph of the real-time X-ray CT system (Duan et al., 2019), and (c) CT images of mudstone samples containing a pre-existing flaw (Lu et al., 2021).

rocks (Li et al., 2020), indicating that there is no clear relationship between the rock type and the normalized crack initiation stress.

2.4. Crack damage stress

The crack damage stress is widely used as an useful indicator for evaluating the long-term strength of practical engineering (Martin, 1997). From Fig. 3, the crack damage stress is related to the UCS and generally presents a monotonic increasing trend. The ratio of crack damage stress to UCS is 0.79 for igneous rocks, 0.81 for metamorphic rocks, and 0.82 for sedimentary rocks, respectively (Li et al., 2020). The dramatic increase in acoustic emission (AE) event numbers indicates that the crack density or internal damage in rocks increases considerably after the axial stress exceeds the damage stress (Cai et al., 2004). The sliding deformation along closed cracks might be one driven factor for the increasing volumetric strain and crack damage stress (Martin and Chandler, 1994).

3. Measurement for experiments on pre-cracked rocks

The acquisition and analysis of quantitative data are extremely important for understanding the mechanical characteristics and failure mechanism of pre-cracked rocks under compression. However, at experimental preparation stage, it is difficult to ensure the position where conventional strain gages should be attached due to the uncertain crack propagation paths (Zhao et al., 2016; Yang et al., 2019). Additionally, the information captured during the loading process is quite finite using strain gages. To address the above issues, the nondestructive monitoring devices and optical techniques have been used to study the detailed failure process of pre-cracked rocks.

3.1. AE and ultrasonic measurement

The property of elastic waves would change when rocks are subjected to compressive loading, which could be used to detect internal damage and investigate failure mechanism of rocks (Lockner, 1993). To date, two nondestructive techniques have been widely adopted for testing pre-cracked samples, i.e. AE technique and ultrasonic measurement. In the AE technique, elastic waves emitted from microcracks could be detected by transducers attached on sample surfaces (Ishida et al., 2017), and the AE signal parameters captured during experiments can be used to quantitatively characterize the rock failure process (Eberhardt et al., 1997, 1998). By analyzing the AE parameters, the cracking and failure processes of granite samples containing two flaws were classified into eight stages (Moradian et al., 2016). Based on the difference in arrival time for elastic waves propagating from source location to transducers, the hypocenter location of microcrack initiation can be determined using localization algorithms (Baxter et al., 2007; Kundu, 2014). To intuitively investigate the cracking processes, the locations of AE hypocenters in samples containing two flaws were calculated (Wang et al., 2021a). After obtaining the location information, the focal mechanism of sources was determined using the polarity technique or moment tensor inversion (Graham et al., 2010). The stress-induced cracks were described as tensile, shear or mixed-mode cracks (Ohno and Ohtsu, 2010). Wong and Xiong (2018) investigated the crack type in Carrara marble with one flaw under uniaxial compression, and they thought that the

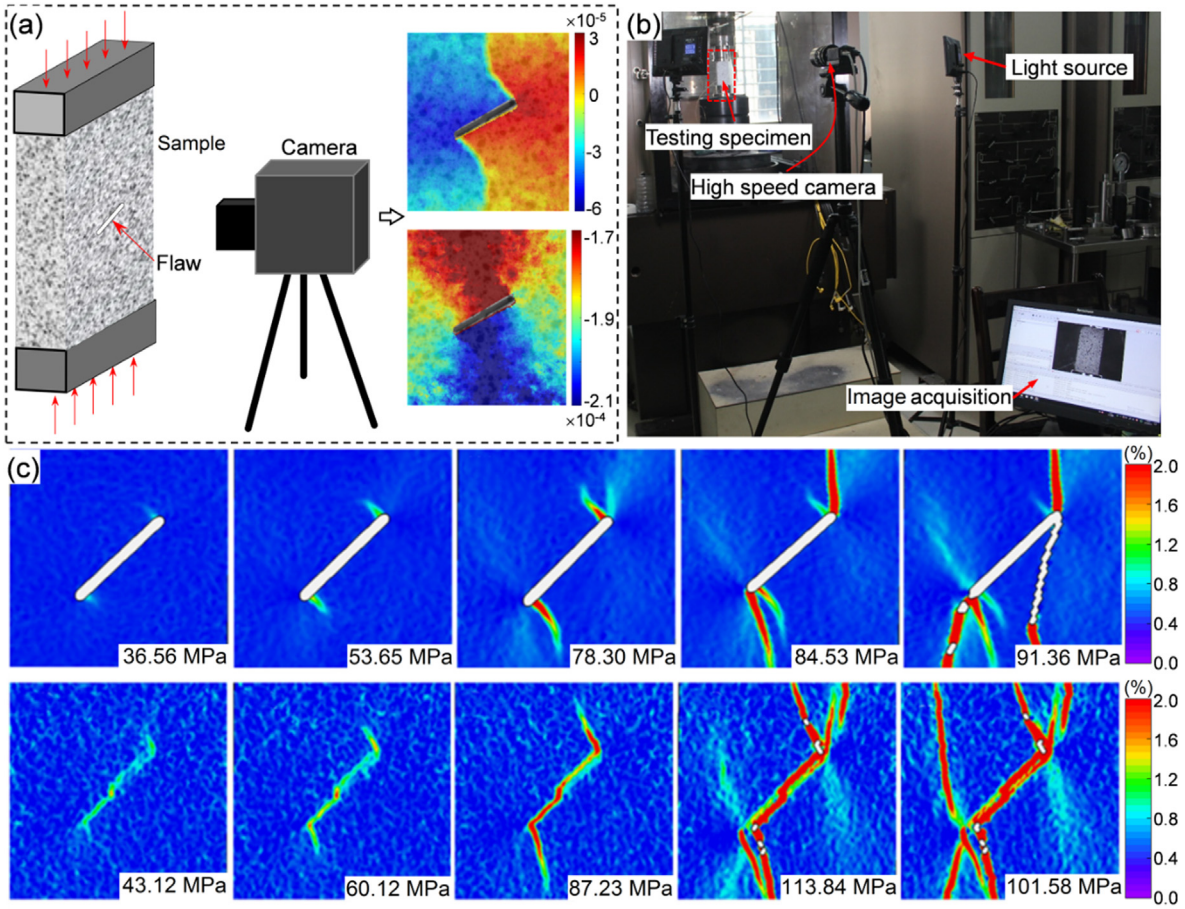

Fig. 5. DIC technique and the experimental results for pre-cracked samples: (a) Schematic diagram of DIC technique (Liu et al., 2021b), (b) Experimental setup used by Liu et al. (2020a), and (c) Major strain contours for samples with one flaw (Pan et al., 2020).

clustering AE events consist of microcracks with tensile, shear and mixed-mode focal mechanisms. In the ultrasonic measurement, elastic waves emitted from transmitters were recorded by receivers, and the wave velocity was calculated by the pulse transmission method (Fortin et al., 2006). By analyzing the difference in wave velocity, the internal damage induced by microcracks was studied, and the rock damage threshold was evaluated as well (Shirole et al., 2020, 2021). From the results of ultrasonic measurement for sandstone with one flaw, the crack initiation would decrease the wave amplitude (Garg et al., 2019). Similarly, Modiriasari et al. (2017) indicated that the initiation of tensile cracks would decrease the amplitude of transmitted waves, while the wave velocity is insensitive to shear crack initiation. The wave amplitude gradually increases with the propagation and coalescence of shear cracks, which has the potential to evaluate damage state in the field (Modiriasari et al., 2020).

3.2. X-ray computed tomography (CT)

Based on the X-ray penetration ability and computerized transverse axial tomography (Cnudde and Boone, 2013), X-ray CT can obtain projection images and material internal features. As presented in Fig. 4a, a collimated fan beam emitted from the X-ray source penetrates through an object at the rotating stage, then the beam would be received by a linear array detector (Flannery et al., 1987). Due to the difference in material property, X-ray intensity would be attenuated, and the attenuation coefficient can be used to back-project the material internal images (Johns et al., 1993). Using reconstruction algorithms (Feldkamp et al., 1984; Ketcham and Carlson, 2001), the internal property in this object can be calculated, including microcrack geometries, pore characteristics, density, displacement, and strain fields (Hall et al., 2010; Sufian and Russell, 2013; Maire and Withers, 2014). To consider the effect of temporal variation, a real-time X-ray CT system (Fig. 4b) was developed to obtain the progressive fracturing process and damage evolution of rocks during experiments. The crack initiation, propagation and coalescence processes of samples containing flaws were experimentally investigated using the X-ray CT technique (Kou et al., 2019; Cao et al., 2020; Wang et al., 2020c; Huang et al., 2021). As illustrated in Fig. 4c, the images of crack growth in mudstone samples with a single flaw were obtained using a real-time CT scanning system, and the crack initiation and propagation characteristics at three deformation stages were determined (Lu et al., 2021).

3.3. Digital image correlation (DIC)

DIC is one of the image processing methods, which can obtain displacement and strain fields in a noncontact manner (Pan et al., 2009). Before testing, sample surface should be covered by speckle patterns with a random intensity distribution to meet the DIC calculation requirements (Lecompte et al., 2006). The speckle patterns include natural texture pattern and artificial speckle pattern, and the pattern quality significantly affects the accuracy of the DIC results (Dong and Pan, 2017). Based on systematic experiments, the optimal speckle diameter is around 4 pixels, and the speckle density

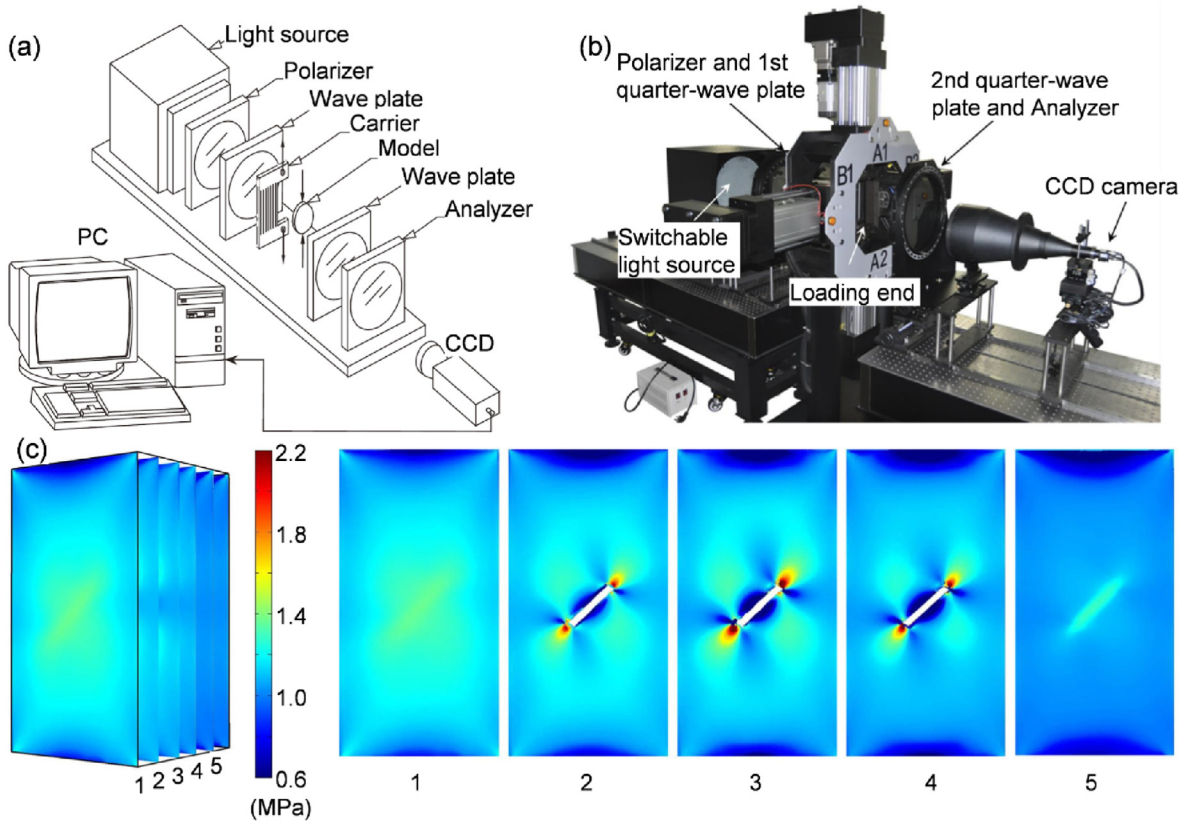

Fig. 6. Digital photoelastic technique and the experimental results for pre-cracked samples: (a) Schematic diagram of the digital photoelastic technique (Ajovalasit et al., 2007), (b) Photo of digital photoelastic apparatus used by Ju et al. (2020), and (c) Full-field principal stress distribution of transparent samples containing an embedded flaw (Ju et al., 2021).

is recommended at 60% (Wang et al., 2021b). Utilizing the image capture devices, such as high-speed camera or scanning electron microscopy technique (Kammers and Daly, 2013; Xing et al., 2018), the continuous deformation images were recorded and stored for post-processing (Fig. 5a). During the DIC analysis process, the region of interest (ROI) was defined in the captured images, and then divided into many subsets. These subsets contain many pixels which can be used for distinguishing themselves from others (Pan et al., 2009). To determine the correlation degree of subsets between reference and deformed images, the correlation criteria were developed (Grün, 1985; Giachetti, 2000; Pan et al., 2010). When the position with the maximum correlation coefficient was determined, the relationship between the reference and deformed images was identified, and the full-field displacement and strain could be subsequently calculated (Blaber et al., 2015). To date, the DIC method has been widely utilized for investigating the cracking process of pre-cracked samples by analyzing full-field strain evolution (Yin et al., 2014; Zhao et al., 2019; Lei et al., 2020; Yan et al., 2020, 2021). When the external stress was applied to pre-cracked samples, strain localization (SL) phenomenon occurred around the flaw. The later formed SL zones had certain impacts on the evolution of pre-existing SL zones, indicating that crack arrest might appear due to the interaction between adjacent stress-induced cracks (Liu et al., 2020a). As illustrated in Fig. 5c, the later formed SL zone reduced the major strain of SL zone formed before, and the crack initiation stress and the failure pattern were influenced by flaw conditions (Pan et al., 2020). By observing the distribution of shear and tensile SL zones, three crack coalescence modes, i.e. shear coalescence, tensile coalescence and mixed coalescence modes, were determined (Zhao et al., 2018).

3.4. Digital photoelastic technique

As one of the optical measurements, digital photoelasticity can extract information about the full-field stress distribution by analyzing the fringe patterns (Ramesh and Sasikumar, 2020). In the fringe pattern, isochromatic and isoclinic data evaluated from image intensity can be utilized to determine principal stress magnitude and direction (Sarma et al., 1992). Fig. 6a presents the detailed equipment information for the digital photoelastic technique, which consists of light source, polarizer, wave plates, model and analyzer. The investigated model should be transparent photosensitive materials with birefringent characteristics, such as photopolymer (Ju et al., 2019), glass (Ramesh and Ramakrishnan, 2016), and resin (Ju et al., 2018). For opaque materials, carrier fringes could be attached on material surface, but the effect was not good enough for conducting photoelastic analysis (Ajovalasit et al., 2007). When the nonpolarized light emitting from the source penetrates through a series of optical apparatus and reaches the charge-coupled device (CCD) camera, model images with fringe patterns can be captured and transferred to the computer (Fig. 6b). Then, the pattern can be analyzed using several assisting methods, including the Fourier transform approach, phase shifting and spectral analysis (Petrucci, 1997; Ajovalasit et al., 1998; Barone et al., 2002). Based on this technique, the investigation on pre-cracked samples with various flaws has been conducted (Lee and Ravichandran, 2003; Patil et al., 2017), and the processes for crack initiation and propagation were studied under uniaxial compression by analyzing the fringe patterns. The reliability of the Griffith theory for an open crack and the reliability of the sliding crack model for a close crack were discussed (Hoek and Bieniawski,

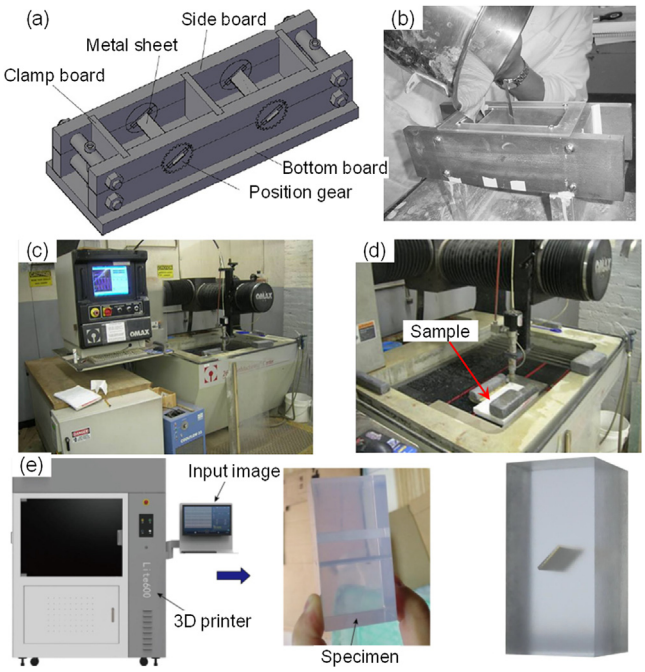

Fig. 7. Methods for fabricating pre-existing flaws: (a) Mold utilized in the casting method, (b) Pour casting materials into the mold; (c) Water-jet machine for fabricating flaws, (d) Fabricating flaws in marble samples, and (e) 3D printer and pre-cracked specimen, reproduced with permission from MIT Libraries (Wong, 2008; Brooks et al., 2013; Zhuang et al., 2014; Liu et al., 2020b; Huang et al., 2021).

1984). In terms of samples containing two flaws, the effect of confining pressure on crack interaction was studied, and the stress intensity factor (SIF) was calculated (Vivekanandan and Ramesh, 2019). Furthermore, the PMMA samples containing multiple flaws were prepared for biaxial compressive tests, and the isoclinic fringe, principal stress orientation and trajectories were analyzed by the digital photoelasticity to understand complex failure patterns (de Joussineau et al., 2003). As to the spatial distribution of stress, the 3D photoelastic technique combining with stress-freezing method was developed (Wijerathne et al., 2008). In this method, models were heated under the stress freezing temperature and slowly cooled to room temperature, and then the optical characteristics of models can be fixed. By obtaining slices of frozen stress models, the full-field stress distribution could consequently be analyzed from a 3D viewpoint (Swain et al., 2016). As presented in Fig. 6c, the full-field internal stress of resin samples containing an embedded flaw was obtained, and the crack initiation and propagation processes could be visually analyzed (Ju et al., 2021).

4. Mechanical characteristics and crack initiation pattern of rocks containing a flaw

4.1. Sample preparation technique

To fabricate pre-existing flaws, three methods were mainly adopted in the laboratory, including casting (Zhuang et al., 2014; Liu et al., 2017), cutting (Wong and Einstein, 2006) and 3D printing (Sharafisafa et al., 2018, 2019; Aliabadian et al., 2021) (Fig. 7). In the casting method, raw materials are mixed and poured into a specific mold with sheets. The mold and sheets have the same dimensions as the designed size of samples and flaws. The material utilized in this method includes gypsum, mortar, and rock-like materials. The sheet includes metal, PMMA sheets and silicon carbide discs. It is difficult to obtain pre-existing flaws in natural rocks using the casting method, thus the cutting method was utilized. The cutting tools include OMAX abrasive jet, water-jet cutting machine, and silicon carbide disc. To date, numerous rock materials have been prepared for experiments, including sandstone, marble, granite and coal. (Wang et al., 1987; Li et al., 2005; Wong and Einstein, 2006, 2009a; Yang and Jing, 2011). As a modern and innovative

Table 1
Summary of samples with a pre-existing flaw in the laboratory.

Material	α (°)	L_f (mm)	W_f (mm)	Prefabrication tool	Source
Gypsum	45	20–25	1	Silicon carbide disc	Wang et al. (1987)
Gypsum	15, 30, 45, 60, 75	14	w/o	Aluminum sheet	Zhao et al. (2019)
Rock-like material	18, 36, 54, 72	50.8	1.98	Steel sheet	Maji et al. (1991)
Rock-like material	15, 30, 45, 60, 75	15	1	Metal sheet	Zhuang et al. (2014)
Rock-like material	0, 15, 30, 45, 60, 75, 90	25	1	PMMA sheet	Lin et al. (2019a)
Rock-like material	0, 30, 45, 60, 90	20	w/o	Water-jet cutting machine	Wang et al. (2019a)
Rock-like material	0, 30, 45, 60, 75, 90	20	0.3	Steel sheet	Lee and Jeon (2011)
Mortar	0, 30, 45, 60, 90	20	0.2	Copper sheet	Han et al. (2019)
Rock-like material	0, 15, 30, 45, 60, 75, 90	20	0.4	Steel sheet	Jin et al. (2017)
Glass	60	w/o	w/o	Diamond scriber	Brace and Bombolakis (1963)
PMMA	0, 30, 45, 60, 75, 90	20	1	Water-jet cutting machine	Lee and Jeon (2011)
Marble	45	20–25	1	Silicon carbide disc	Wang et al. (1987)
Marble	30, 45	20	0.5–1	Steel sheet	Li et al. (2005)
Marble	0, 30, 45, 60, 75	12.5	1.3	OMAX abrasive jet	Wong and Einstein (2006, 2009b)
Marble	30, 45, 60	20	1	w/o	Huang et al. (1990)
Marble	30	12.7	1	OMAX abrasive jet	Brooks et al. (2013)
Marble	30, 45, 60, 70, 90	13	1.6	OMAX abrasive jet	Wong and Xiong (2018)
Sandstone	15, 45, 60, 75	5–25	2.5	Water-jet cutting machine	Yang and Jing (2011)
Sandstone	0, 15, 30, 45, 60, 75, 90	25	2	Water-jet cutting machine	Miao et al. (2018)
Sandstone	15, 30, 45, 60, 75	24	1.5	Water-jet cutting machine	Zhu et al. (2016)
Sandstone	45	24	w/o	OMAX abrasive jet	Niu et al. (2020)
Sandstone	0, 30, 60, 90	15	3	w/o	Peng et al. (2019)
Sandstone	15, 30, 45, 60, 75	12	1	Water-jet cutting machine	Li et al. (2019d)
Sandstone	45	16	2	Water-jet cutting machine	Yang et al. (2014)
Granite	0, 15, 30, 45, 60, 75, 90	20	1.5	Water-jet cutting machine	Yang et al. (2019)
Granite	0, 30, 45, 60, 75, 90	20	1	Water-jet cutting machine	Lee and Jeon (2011)
Coal	0, 15, 30, 45, 60, 75, 90	20	2	Steel sheet	Li et al. (2019b)
Resin	30, 45, 60, 75	6	w/o	3D printer	Dong et al. (2020)
Vero Clear	45	30	1	3D printer	Liu et al. (2020b)
Vero Clear	45	15	1	3D printer	Ju et al. (2021)

Note: Vero Clear is a transparent material like PMMA, and w/o means that the data are not given in the sources.

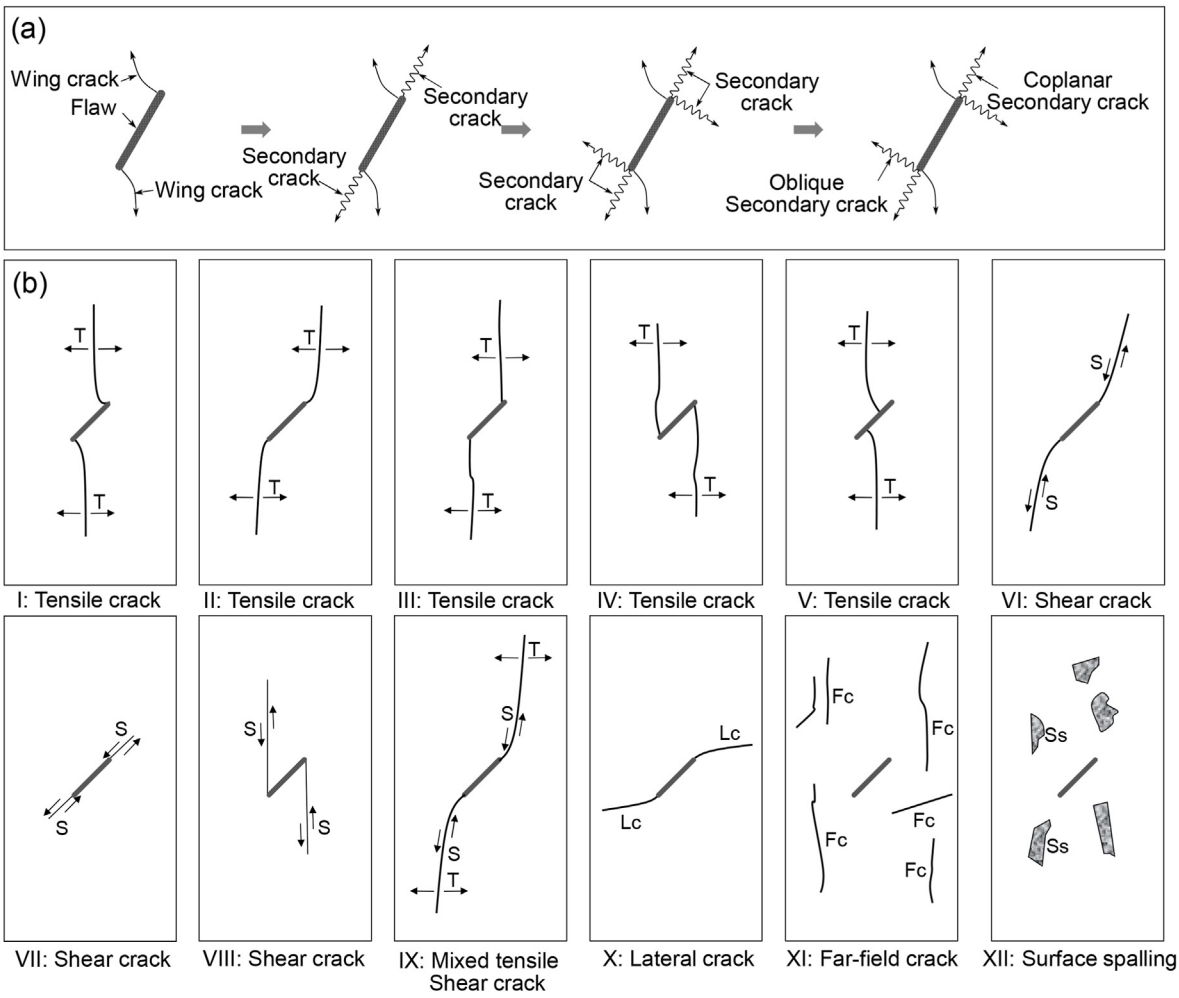

Fig. 8. Crack initiation pattern classified by (a) Crack geometrical characteristics (modified after Brace and Bombolakis, 1963; Lajtai, 1974; Nemat-Nasser and Horii, 1982; Horii and Nemat-Nasser, 1985; Bobet and Einstein, 1998; Bobet, 2000; Park and Bobet, 2009), and (b) Cracking mechanisms. T represents the tensile crack, S represents the shear crack, Lc represents the lateral crack, Fc represents the far-field crack, and Ss represents the surface spalling. Type I–V, VII and X–XII cracks are from Yang and Jing (2011) and type I, II, IV and VI–IX cracks are from Wong and Einstein (2009b).

manufacturing method, the 3D printing technology can repeatedly generate sample models with the same designed microstructure (Jiang and Zhao, 2015). Using images with the standard triangulation language (STL) format, a 3D printer would generate the sample model by accumulating layers with different geometrical information. As displayed in Table 1, the flaw in experiments has different geometrical characteristics. The flaw inclination angle α changes from 0° to 90°; the flaw length L_f changes from 5 mm to 50.8 mm; and the flaw width W_f changes from 0.2 mm to 2.5 mm. Flaw inclination angle is the angle between pre-existing flaw and the direction perpendicular to axial loading direction.

4.2. Crack initiation pattern

Fig. 8 illustrates the progressive process for understanding crack initiation pattern during the last few decades. Based on crack initiation sequence and geometrical characteristics, the stress-induced cracks initiating from flaws can be divided into wing cracks and secondary cracks (Lajtai, 1974; Nemat-Nasser and Horii, 1982; Horii and Nemat-Nasser, 1985; Bobet and Einstein, 1998). According to the difference in crack propagation paths, secondary cracks can be further classified into coplanar and oblique secondary cracks (Bobet, 2000; Sagong and Bobet, 2002; Park and Bobet, 2009). The wing crack is usually the first crack initiated from flaw tips, and thus it is commonly known as the primary crack (Wong and Einstein, 2009b). As the compressive stress is gradually applied, the wing cracks stably propagate following a curvilinear path, which progressively becomes parallel with the direction of the maximum compressive loading. In contrast, the initiation of secondary cracks is later than that of the wing cracks. They propagate stably at the beginning and may be unstable when the failure is about to occur. The coplanar secondary crack with a small inclination angle initiates from the flaw tips and propagates nearly along the inclination direction of the pre-existing flaw. The oblique secondary crack has a large inclination angle, and its initiation direction is oblique against pre-existing flaws. Additionally, the oblique secondary crack is known as anti-wing crack since its propagation path is in the opposite side of wing cracks (Zhuang et al., 2014).

By observing crack surfaces of tested samples, the above crack initiation pattern can be further identified as tensile cracks, shear cracks, and mixed tensile/shear cracks. The tensile crack surface is relatively clean and characterized by a plumose structure. The shear crack surface is rough due to the covering pulverized powder, and the shear crack initiation process is violently accompanied by surface spalling phenomenon (Bobet and Einstein, 1998; Wong and Einstein, 2006, 2009a; Park and Bobet, 2009; Lee and Jeon, 2011). It might be insufficient to determine the cracking mechanism of

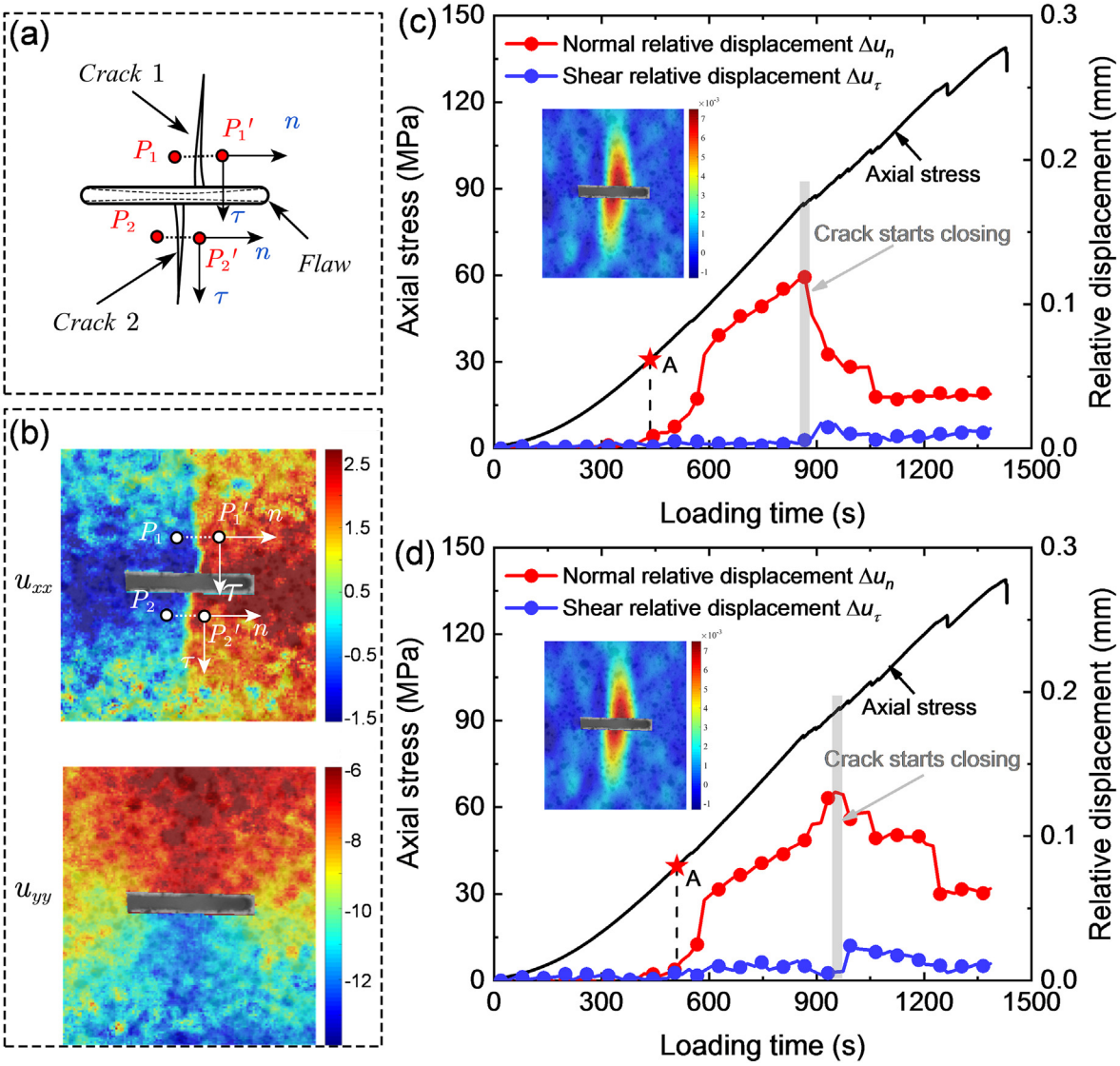

Fig. 9. Experimental results for quantitatively determining the crack initiation mechanisms of pre-cracked sample with inclination angle of 0°: (a) Sketch of cracks initiated from flaw, (b) Distribution of full-field displacements in global coordinate, and relative displacements along the normal and shear directions of (c) Crack 1 and (d) Crack 2 (Liu et al., 2021b).

pre-cracked rocks by observing crack surfaces, because the pulverized powder might be caused when the crack initiates in tension and then the surfaces slip against each other (Reyes and Einstein, 1991). To better investigate the crack initiation mechanism of the stress-induced cracks, Wong and Einstein (2009a) and Yang and Jing (2011) timely monitored the tensile and shear deformation around cracks using a high-speed camera. Twelve types of crack initiation patterns were accordingly obtained, including five of tensile cracks, three of shear cracks, one of mixed tensile/shear crack, one of lateral crack, one of far-field crack, and one of surface spalling crack (Fig. 8b). To reduce the influence of human judgment, Liu et al. (2021b) innovatively proposed a quantitative method to determine the crack initiation mechanism using the DIC method. Fig. 9 shows the results for quantitatively determining the crack initiation mechanism of pre-cracked sample with inclination angle of 0°. By setting two monitoring points around the stress-induced cracks, the change of relative displacements along the normal and shear directions during compression can be obtained after displacement transformation. It is apparent that the normal relative displacement increases dramatically, while the change of shear relative displacement is marginal. Therefore, the Cracks 1 and 2 are regarded as mode I cracks, which are mainly induced by tensile stress. For sample containing one flaw, wing cracks are mainly identified as mode I cracks and mixed mode I-II cracks, and the mode II cracks are the dominant mechanism for anti-wing cracks. With the increasing of flaw inclination angle, the underlying mechanism for anti-wing crack initiation do not change, whereas a transition between mixed mode I-II cracks to mode I cracks appears for the initiation mechanism of wing cracks.

4.3. Influences of flaw geometry and loading condition

4.3.1. Flaw inclination angle

Fig. 10 displays the mechanical characteristics of rocks containing one flaw under compression. The characteristics of pre-cracked samples with different flaw angles were normalized by these of intact rocks. Evidently, the flaw significantly degrades the mechanical properties of rocks, including peak strength, peak strain and elastic modulus (Liu et al., 2021a). As for samples with small inclination angle α, the degradation effect is obvious. The

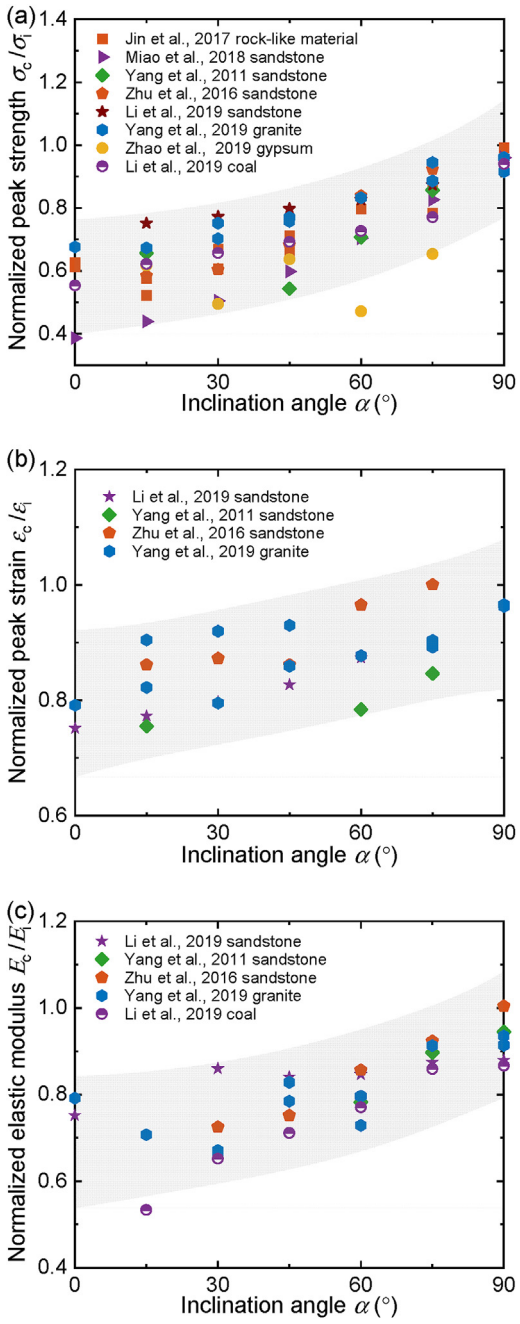

Fig. 10. Effect of flaw inclination angle on mechanical characteristics of pre-cracked rocks containing a flaw: (a) Normalized peak strength, (b) Normalized peak strain, and (c) Normalized elastic modulus (data from Yang and Jing, 2011; Zhuang et al., 2014; Zhu et al., 2016; Jin et al., 2017; Miao et al., 2018; Li et al., 2019b, d; Yang et al., 2019; Zhao et al., 2019, see Table A1-A3 in Appendix A). Symbols c and i represent the pre-cracked and intact samples, respectively.

mechanical properties present increasing tendencies with the increase in inclination angle. When the flaw angle α approaches 90°, the corresponding normalized value approaches 1. To obtain the underlying mechanism, Peng et al. (2019) analyzed the energy evolution of pre-cracked rocks with different inclination angles. Their results indicated that the energy release capacity of rocks containing a single flaw becomes weaker with increasing inclination angle. Utilizing the DIC method, Liu et al. (2020a) found that the upper and lower flaw surfaces would deform towards each other under compression. As the inclination angle increases, the flaw deformation becomes difficult, leading to an increase in the mechanical properties.

The crack initiation phenomenon of pre-cracked samples is easy to observe in the laboratory. As illustrated in Fig. 11, the angle between the crack initiation direction and the pre-existing flaw is defined as the crack initiation angle β. The increase in the flaw inclination angle α can generally increase the crack initiation stress, which makes the material possess a better ability to resist external loads. The crack initiation stresses of pre-cracked samples were normalized by their peak strengths. The crack initiation angle β generally presents a decreasing tendency, revealing that the initiation point moves from the flaw center to the flaw tips (Wu and Chang, 1978; Li and Wong, 2012; Zhang and Wong, 2012; Euser et al., 2019).

4.3.2. Flaw length

It is widely recognized that the mechanical characteristics are dependent on the sample size as evidenced by a decreasing UCS with the increasing sample size. This phenomenon is termed the "size effect" (del Viso et al., 2008). Fig. 12 shows the mechanical characteristics of pre-cracked samples containing a pre-existing flaw with various lengths. The mechanical characteristics of pre-cracked samples were normalized by these of intact samples. The flaw length L_f changes from 5 mm to 30 mm with an increment of 5 mm, and the inclination angle α and width W_f keep unchanged (i.e. $\alpha = 45°$ and $W_f = 2.5$ mm). The increase in flaw length leads to the degradation of UCS, peak strain and elastic modulus of pre-cracked samples. The flaw under compression could be regarded as a

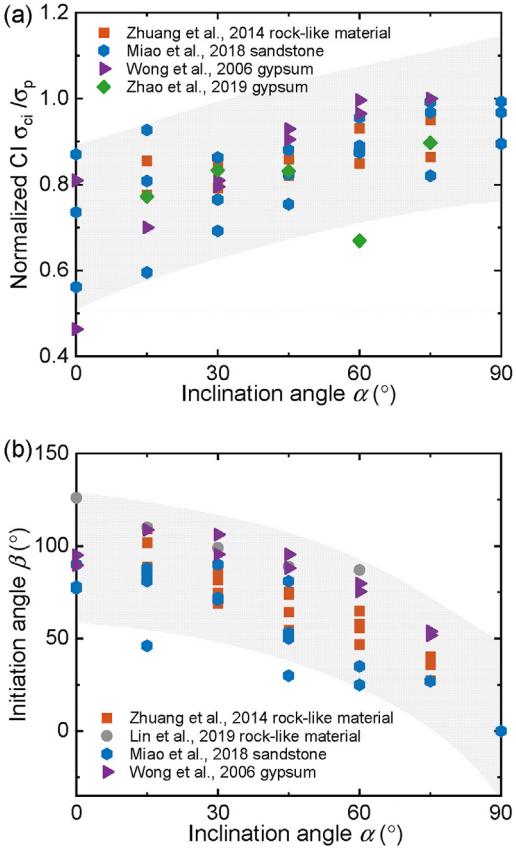

Fig. 11. Crack initiation stress and crack initiation angle of pre-cracked samples containing a single flaw with different inclination angles: (a) Normalized crack initiation stress, and (b) Crack initiation angle (data from Wong and Einstein, 2006; Zhuang et al., 2014; Miao et al., 2018; Lin et al., 2019b; Zhao et al., 2019, see Table A4 in Appendix A).

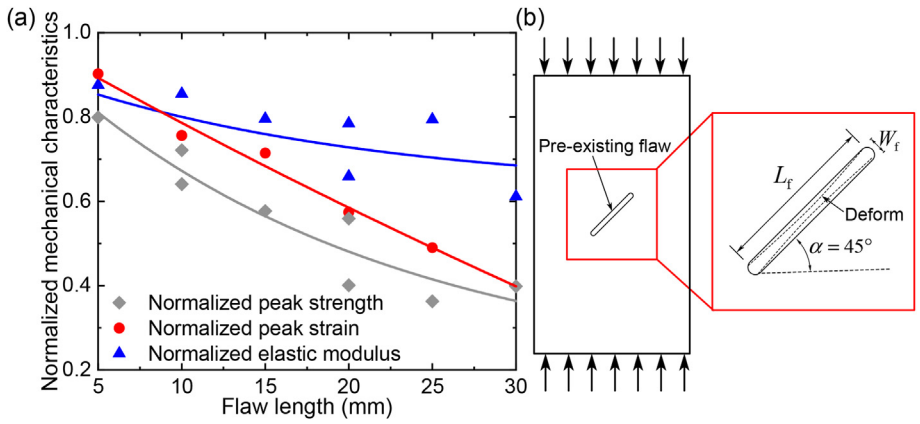

Fig. 12. Effect of flaw length on mechanical characteristics of pre-cracked samples containing a flaw: (a) Normalized mechanical characteristics (data from Yang and Jing, 2011; Le et al., 2018), and (b) Schematic diagram of sample dimensions and flaw deformation.

simple beam, in which the upper and lower surfaces would deform towards each other (Fig. 12b). When the beam length increases, the surface deformation becomes larger, and thus the crack initiation becomes easier, and the mechanical parameters consequently decrease.

4.3.3. Flaw width

According to the difference in flaw width, the flaws can be divided into two types, i.e. the non-frictional/open flaw and frictional/closed flaw. The above two types of flaws are respectively relative to the Griffith crack model and the sliding crack model in theoretical analysis (Lajtai, 1971; Nemat-Nasser and Horii, 1982; Horii et al., 1986). The flaw with surface contact or friction is defined as frictional/closed flaw, and that without surface contact or friction is defined as non-frictional/open flaw (Wong and Chau, 1998). As shown in Fig. 13, the wing cracks, coplanar and oblique secondary cracks could initiate from the tips of open and closed flaws. Normal and shear stresses in samples can be transferred by closed flaws, and thus the initiation stress of cracks emanating from closed flaw is greater than that from open flaws. However, the crack initiation angle in samples with closed flaws is smaller. Under same compressive loading, wing cracks initiated from open flaws have larger length and width (Wong and Einstein, 2006; Park and Bobet, 2009).

4.3.4. Flaw filling condition

Discontinuity could be filled by different minerals to form a vein or natural fracture with a certain thickness. The deformation of veins or natural fractures could result in the failure of rock structures, even inducing engineering disasters. Therefore, a series of experiments has been recently conducted to study the influence of filling conditions on the mechanical characteristics and cracking behavior of pre-cracked samples (Zhao, 2004; Zhuang et al., 2014; Miao et al., 2018; Yuan et al., 2018; Pan et al., 2020). As shown in Table 2, the fillers mainly include gypsum, cement and resin.

Fig. 14 shows the mechanical properties and crack initiation behavior of pre-cracked samples with one flaw filled by different materials. The peak strengths of pre-cracked samples were normalized by that of intact samples. The crack initiation stresses of pre-cracked samples were normalized by peak strength. With the increase of inclination angle, the peak strength and crack initiation stress generally increase, while the crack initiation angle generally

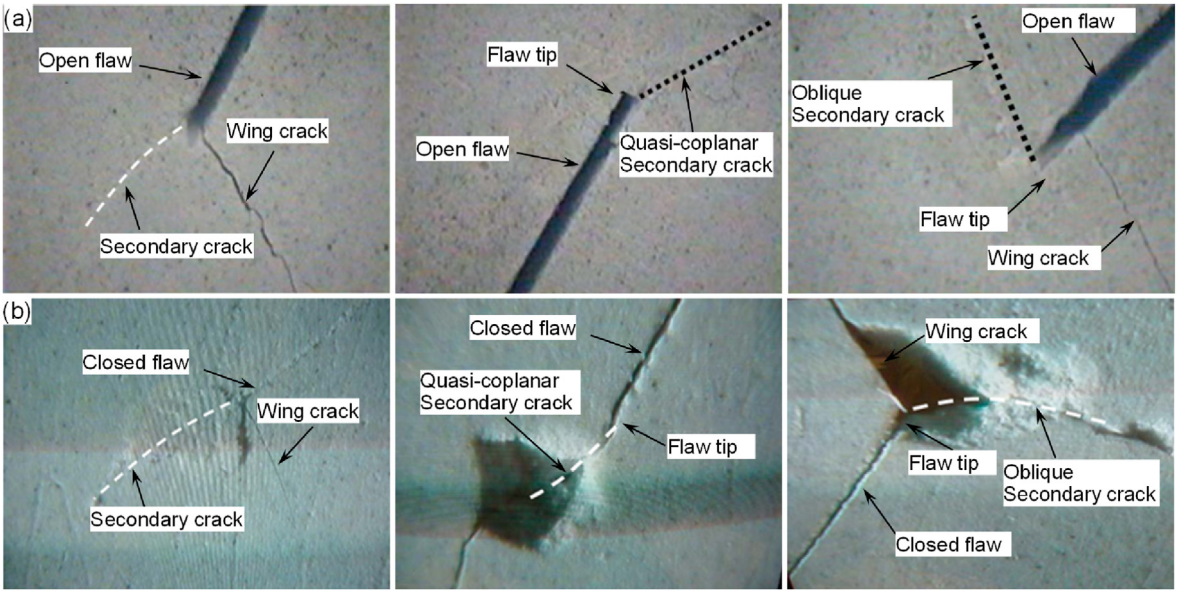

Fig. 13. Crack initiation pattern observed in samples containing (a) open and (b) closed flaws (Park and Bobet, 2009).

Table 2
Summary of the characteristics of pre-existing flaw filled by different materials.

Material	α (°)	L_f (mm)	W_f (mm)	Filler	Source
Rock-like material	15, 30, 45, 60, 75	15	1	Gypsum	Zhuang et al. (2014)
Sandstone	0, 15, 30, 45, 60, 75, 90	25	2	Gypsum Cement Resin	Miao et al. (2018)
Marble	0, 15, 30, 45, 60, 75, 90	25	2	Gypsum Cement Resin	Pan et al. (2020)
Marble	30, 45, 60	5.5, 6, 6.4	w/o	Cement	Zhao (2004)
Marble	45	w/o	w/o	Cement	Zhao and Yang (2005)
Marble	30, 45, 60	30	2	Gypsum Cement Resin	Yuan et al. (2018)
Sandstone	0, 30, 45, 60, 90	24	w/o	Gypsum	Zhou et al. (2021a)
Granite	0, 15, 30, 45, 60, 75, 90	10	1.5	Gypsum Silicone Resin	Wang et al. (2020d)
Sandstone	0, 30, 45, 60, 90	20	1	Ice	Shan et al. (2021)
Sandstone	0, 30, 45, 60, 90	w/o	3	Gypsum	Gong et al. (2021)

decreases. Compared with unfilled samples, the filled samples have larger values of peak strength and crack initiation stress. It is because that the filler can transfer stress and weaken the stress concentration around flaw tips (Zhao and Zhou, 2016). Additionally, the peak strength and crack initiation stress of samples with a flaw filled by different materials have the following relationship: resin

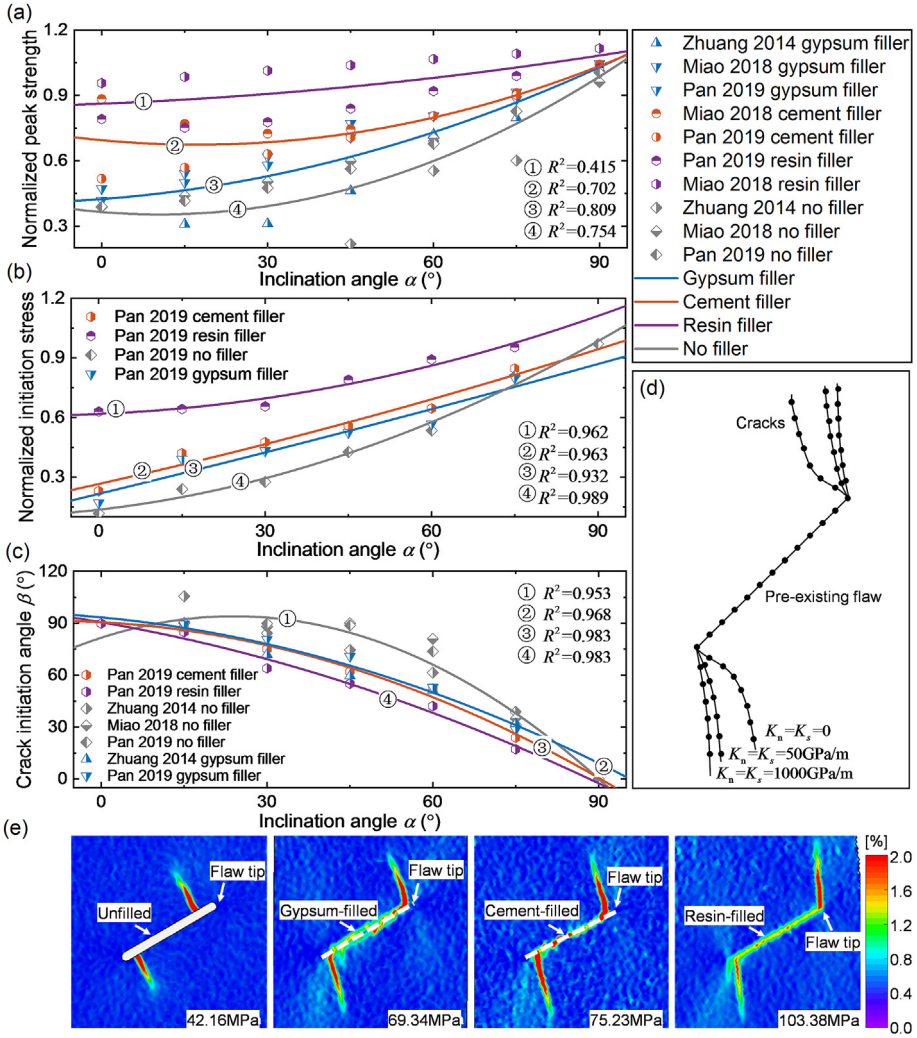

Fig. 14. Mechanical characteristics and crack initiation behavior of pre-cracked samples containing a flaw filled by different materials: (a) Normalized peak strength (data from Zhuang et al., 2014; Miao et al., 2018; Pan et al., 2020), (b) Normalized crack initiation stress, (c) Crack initiation angle, (d) Numerical results under different contact conditions, reproduced with permission from AGU (Shen et al., 1995), and (e) Major strain contours of samples filled by different materials when crack initiates (Pan et al., 2020).

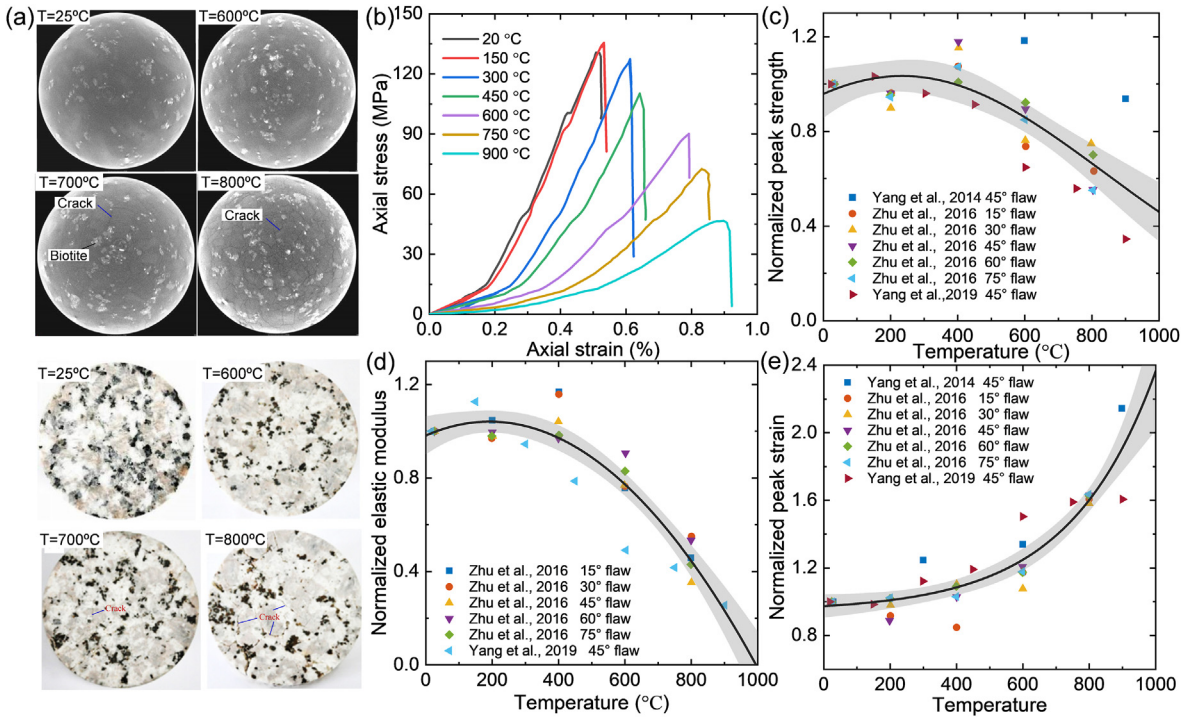

Fig. 15. Effect of temperature on mechanical characteristics of rock materials: (a) Macroscopic and microscopic cracks after thermal treatment (Yang et al., 2017a), (b) Axial stress-strain curves of granite containing a single flaw (Yang et al., 2019), (c) Normalized peak strength as a function of temperature, (d) Normalized elastic modulus concerning temperature, and (e) Normalized peak strain as a function of temperature (Yang et al., 2014, 2019; Zhu et al., 2016).

filler > cement filler > gypsum filler, while the crack initiation angle is in a reverse order. As illustrated in Fig. 14e, the deformation of lower and upper flaw surfaces is related to the type of filling materials. With increasing material stiffness, the normal and shear deformation is difficult to occur, which restrains the crack initiation and decreases the crack initiation angle. In addition, the crack initiation and propagation in filled samples become similar with the ideal slide crack model. The quasi-coplanar cracks are easy to appear, but the initiation of anti-wing cracks is constrained (Pan et al., 2020). Utilizing the displacement discontinuity method to

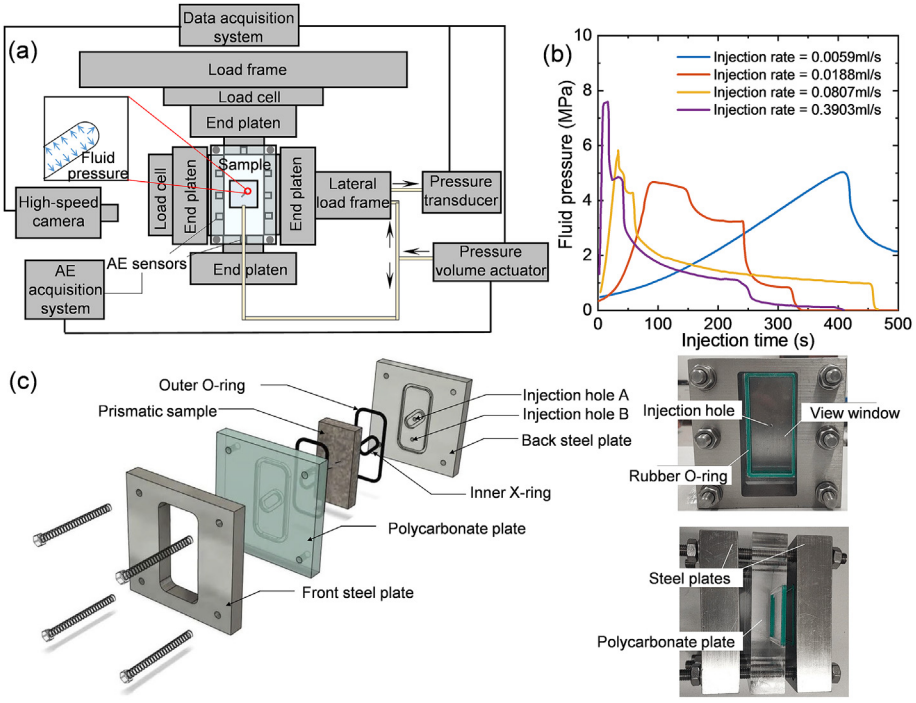

Fig. 16. Experimental apparatus for hydraulic fracturing of pre-cracked samples and the experimental results: (a) Equipment for hydraulic fracturing (modified after Morgan et al., 2017), (b) Fluid pressure as a function of the injection time (Morgan et al., 2017), and (c) Fluid pressure enclosure (Zhao et al., 2020; Gunarathna and Gonçalves da Silva, 2021).

mimic samples containing pre-existing flaws with different contact conditions, Shen et al. (1995) found that the increases of normal and shear stiffnesses result in the decrease of crack initiation angle, and the cracking path changes from curve to nearly straight line (Fig. 14d). Based on the numerical results obtained by rock failure process analysis, there exists a critical strength of filling material for influencing the mechanical characteristics and crack initiation of rocks. When the filler strength is smaller than the critical value, the initiations of secondary and anti-wing cracks become difficult with the increase of filler strength (Chang et al., 2018).

4.3.5. Confining pressure

It is commonly accepted that the confining pressure has a great impact on the mechanical characteristics of rock materials. As the confining pressure increases, the peak strength of rocks presents an increasing trend. Brittle-ductile transition phenomenon occurs, and the failure pattern of rocks gradually changes from axial tensile splitting to shear fracture. To facilitate the observation of cracking process, biaxial compressive tests in conjunction with a high-speed camera were usually conducted on prismatic rock samples containing flaws. Wing and secondary cracks identified in uniaxial compression tests are observed in biaxial compression tests as well. The initiation position of wing cracks moves towards the flaw center, and the peak strength presents an increasing tendency as the confining stress increases (Bobet and Einstein, 1998; Liu et al., 2016, 2019; Fu et al., 2018). When the confining stress exceeds a critical value, the wing cracks become difficult to initiate and even disappear (Bobet and Einstein, 1998). Based on numerical simulations, the tensile stress concentration around flaws is weakened with the increase of confining stress, preventing the initiation of wing cracks (Manouchehrian et al., 2014; Wan et al., 2019).

4.3.6. Thermal treatment

Rock materials in the Earth's crust have experienced a series of geological processes, including high temperature treatment (Heuze, 1983). Therefore, investigating the effect of temperature on the mechanical characteristics is of great significance for engineering construction, such as nuclear waste disposal (Wang, 2010), and geothermal exploitation (Henley and Ellis, 1983). Rock components respond differently to high temperature, which results in microstructure change and influences the macroscopic mechanical characteristics (Nasseri et al., 2007; Tian et al., 2017). For instance, minerals subjected to temperature treatment would exhibit thermal expansion, resulting in the formation of microcracks and thermal damage (Sirdesai et al., 2019). With the increase of thermal-induced microcracks, stress-induced cracks become easier to coalesce, which consequently degrades the mechanical characteristics (Homand-Etienne and Houpert, 1989). As illustrated in Fig. 15, the treatment under high temperature leads to the generation of microcracks and has a severe influence on the stress-strain curves for samples containing a single flaw (Yang et al., 2014, 2017a, 2019; Zhu et al., 2016). The mechanical characteristics were normalized by the corresponding values at the room temperature. From the results of CT scanning and direct observation, the crack density after thermal treatment presents an increasing trend (Fig. 15a). When the temperature changes in the range of 25 °C–1000 °C, the normalized peak strain generally increases from 1 to 2.4, whereas the normalized peak strength and elastic modulus increase and then decrease. The temperature corresponding to the maximum peak strength and elastic modulus is in the range of 100 °C–400 °C (Fig. 15c–e). At the first stage (25 °C–400 °C), water in rocks gradually evaporates, and the expansion of minerals leads to the microcrack closure or the porosity reduction, resulting in the enhancement of peak strength and elastic modulus (Gautam et al., 2018). Due to the expansion mismatch, microcracks and thermal damage appears as the temperature increases. At 573 °C, the phase transition of quartz occurs (Glover et al., 1995).

4.3.7. Fluid pressure

In the field of hydraulic fracturing, fluid has been widely utilized to inject into rock materials, aiming to obtain complex fracture networks and improve the extraction efficiency of oil, unconventional gas or geothermal energy (Soliman et al., 2012; Li et al., 2015). The pressure induced by the permeation of fluid leads to the initiation and propagation of stress-induced cracks, which provides a more convenient path for the transportation of energy media. Based on fluid and fracture mechanics, a series of theoretical crack models has been proposed for describing the behavior of

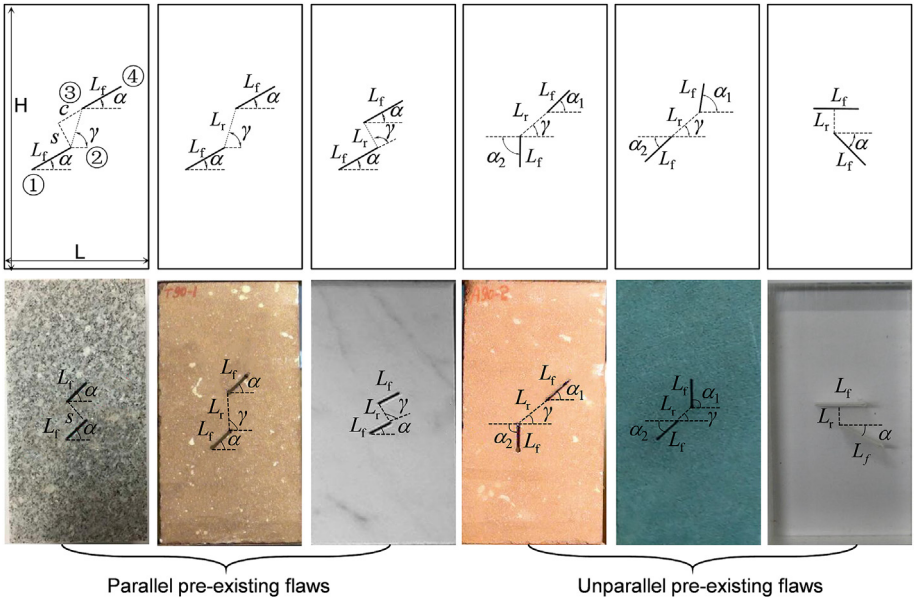

Fig. 17. Summary of the geometry of samples with two flaws (modified after Bobet, 2000; Park and Bobet, 2009; Wong and Einstein, 2009a; Lee and Jeon, 2011; Morgan et al., 2013; Yang et al., 2013, 2014; Modiriasari et al., 2017; Feng et al., 2019; Zhou et al., 2019a, b).

hydraulically induced fractures (Savitski and Detournay, 2002; Adachi et al., 2007; Kovalyshen and Detournay, 2010; Dontsov and Peirce, 2015). To better investigate the behavior of hydraulic cracks, a hydraulic fracturing equipment was invented for testing pre-cracked samples (Gonçalves da Silva and Einstein, 2018; Li and Einstein, 2019; Li et al., 2019a). The equipment has biaxial loading capacities and is convenient for the high-speed camera to record the whole cracking process (Fig. 16a). The crucial element in this equipment is the fluid pressure enclosure, consisting of two pieces of steel plate, one transparent plate, several sealing rings and injection holes. The prismatic samples are sandwiched between the plates, and the fluid is injected into the flaw through the injection holes after the axial and lateral stresses are applied (Fig. 16c). It is evident that the fluid injection rate significantly influences the curves of the fluid pressure and injection time. The breakdown fluid pressure generally increases with the increasing injection rate, and the time corresponding to the breakdown fluid pressure presents an inverse changing trend (Fig. 16b). Fig. 16d illustrates the cracking process of hydraulically induced cracks in shale samples. By observing the cracking process of hydraulically induced cracks in shale samples, two cracks emanating from flaw tips initiated when the fluid pressure increased to 5.61MPa. And the cracks tended to propagate along the direction of horizontal bedding planes (Morgan et al., 2017).

5. Crack coalescence pattern of rocks containing two flaws

5.1. Geometry of pre-existing flaw

Samples with two pre-existing flaws have more complicated flaw geometries, which can be mainly classified into parallel and unparallel flaws. As illustrated in Fig. 17, the inclination angle in parallel pre-existing flaws is the same, while different in unparallel pre-existing flaws. The geometry of flaws can be characterized by flaw inclination angle α, flaw length L_f, rock bridge length L_r, rock bridge angle γ, spacing s, and continuity c. By judging whether the continuity is smaller than zero or not, the pre-existing flaws can be classified into overlapped and non-overlapped flaws. The parallel flaws with the same directions as the rock bridge direction is defined as coplanar pre-existing flaws (Bobet and Einstein, 1998; Bobet, 2000; Park and Bobet, 2009; Lee and Jeon, 2011; Wong and Li, 2013; Tian et al., 2018). Fig. 17 summarizes the geometry of the samples containing two flaws, and a series of experiments has been carried out on such pre-cracked samples, including uniaxial compression and biaxial compression tests (Table 3). The pre-existing flaws in the literature are mostly parallel flaws, and thus the crack coalescence of the samples containing two parallel flaws is analyzed in the following part.

Table 3
Summary of the geometrical characteristics of samples containing two flaws.

Material	Length × width × height (mm × mm × mm)	Geometry	Geometry parameter	Loading condition	Source
Gypsum	152.4 × 76.2 × 30	PF	$L_f = 2a = 12.7$ mm, s = 0-4a@a, $c = a$-4a@a, $\alpha = 30°$ −60°@15°	UC BC	Bobet and Einstein (1998); Bobet (2000)
Gypsum	152.4 × 76.2 × 30	PF	$L_f = 2a = 12.7$ mm, $s = a$-2a, $c = -2a$-4a, $\alpha = 30°$ −60°@15°	UC	Park and Bobet (2009)
Granite	160 × 80 × 27	PF	$L_f = 2a = 8$ mm, $s = 4a$, $c = 0$, $\alpha = 45°$	UC	Zhou et al. (2019b)
Gypsum	152.4 × 76.2 × 30	PF	$L_f = L_r = 12.7$ mm, $\alpha = 30°$−60°@15°, $\gamma = 45°$ −120°@15°	UC	Shen et al. (1995)
Tuff	100 × 50 × 35	PF	$L_f = L_r = 12$ mm, $\alpha = 45°$, $\gamma = 45°$−120°@15°	UC	Hall et al. (2006)
Rock-like material	200 × 150 × 30	PF	$L_f = 20$ mm, $L_r = 40$ mm, $\alpha = 25°$, 45°, 75° $\gamma = 25°$, 45°−105°@15°	UC	Cao et al. (2015); Zhao et al. (2016)
Sandstone	160 × 80 × 30	PF	$L_f = 15$ mm, $L_r = 18$ mm, $\alpha = 30°$, $\gamma = 0°$−120°@30°	UC	Yang et al. (2016)
Shale	100 × 50 × 25	PF	$L_f = L_r = 8.4$ mm, $\alpha = 0°$, 30°−75°@15°, $\gamma = 0°$ −90°@30°	UC	Morgan and Einstein (2017)
Rock-like material	120 × 60 × 25	PF	$L_f = 12$ mm, $L_r = 20$ mm, $\alpha = 35°$−75°@10°, $\gamma = 45°$ −120°@15°	UC	Wong and Chau (1998)
Sandstone	160 × 80 × 30	PF	$L_f = 16$ mm, $L_r = 22$ mm, $\alpha = 45°$, $\gamma = 90°$	UC	Yang et al. (2014)
Gypsum	100 × 40 × 10	PF	$L_f = 14$ mm, $L_r = 21$ mm, $\alpha = 30°$−60°@15°, $\gamma = 90°$, 120°, 180°	UC	Zhao et al. (2018)
Granite	160 × 80 × 30	PF	$L_f = 15$ mm, $L_r = 18$ mm, $\alpha = 30°$, $\gamma = 0°$−120°@30°	UC	Tian et al. (2018)
Rock-like material	300 × 300 × 120	PF	$L_f = 90$ mm, $L_r = 50$ mm, $\alpha = 30°$, 60°, $\gamma = 30°$, 60°, 90°, 115°, 135°	UC	Naderloo et al. (2019)
Granite	152.4 × 76.2 × 25.4	PF	$L_f = L_r = 12.7$ mm, $\alpha = \gamma = 30°$	HF	Li et al. (2019a)
Sandstone	140 × 70 × 70	PF	$L_f = 0$, 20, 30 mm, $L_r = 25$ mm, $\alpha = 45°$, $\gamma = 105°$	UC	Shi et al. (2019)
Sandstone	120 × 60 × 30	PF	$L_f = L_r = 20$ mm, $\alpha = 45°$, $\gamma = 90°$	UC	Li et al. (2019c)
Rock-like material	280 × 185 × 40	PF	$L_f = 20$ mm, $L_r = 40$ mm, $\alpha = 15°$−75°@15°, $\gamma = 15°$ −120°@15°	BC	Wang et al. (2020b)
Marble	152.4 × 76.2 × 30	PF	$L_f = 2a = 12.7$ mm, $L_r = 2a$-4a@2a, $\alpha = 0°$, 30° −75°@15° $\gamma = -60°$-120°@30°	UC	Wong and Einstein (2009a)
Granite	152.4 × 76.2 × 30	PF	$L_f = 2a = 12.7$ mm, $L_r = a$-3a@a, α = w/o, $\gamma = 0°$ −60°@15°	UC	Morgan et al. (2013)
Granite	152.4 × 76.2 × 25.4	PF	$L_f = 12.7$ mm, L_r = w/o, α = w/o, γ = w/o	HF	Gonçalves da Silva and Einstein (2018)
Rock−like material	142 × 72 × 40	PF	$L_f = L_r = 20$ mm, $\alpha = -60°$, 60°, $\gamma = -45°$-45°@45°	UC	Wang et al. (2020a, 2020b, 2020c. 2020d)
Sandstone	160 × 80 × 30	UF	$L_f = 16$ mm, $L_r = 22$ mm, $\alpha_1 = \gamma = 45°$,$\alpha_2 = 0°$ −180°@45°	UC	Yang et al. (2013)
Sandstone	160 × 80 × 30	UF	$L_f = 16$ mm, $L_r = 10$ mm, $\alpha_1 = \gamma = 45°$,$\alpha_2 = 0°$ −180°@45°	UC	Zhou et al. (2019a)
PMMA, Granite	120 × 60 × 25	UF	$L_f = 20$ mm, $L_r = 10$ mm, $\alpha = 30°$−90°@15°	UC	Lee and Jeon (2011)

Note: The number after @ is the increment. UC, BC, HF represent the uniaxial compression, biaxial compression, and hydraulic fracturing, respectively; and PF and UF are abbreviations of parallel and unparallel pre-existing flaws, respectively.

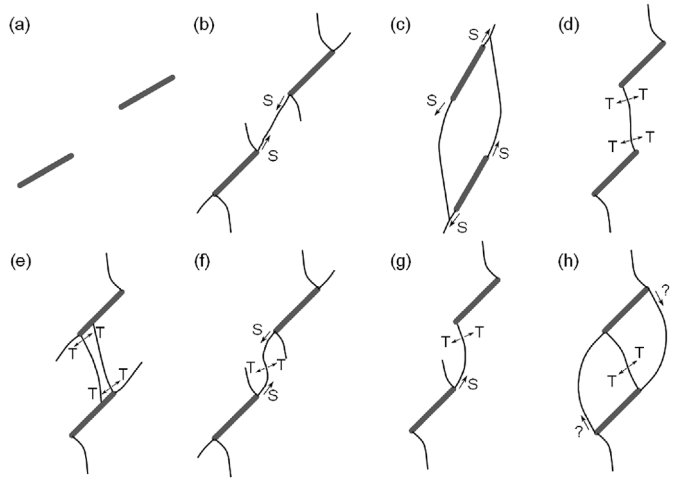

Fig. 18. Schematic diagrams of crack coalescence patterns of samples containing two parallel flaws: (a) No coalescence pattern, (b, c) Shear crack coalescence pattern, (d, e) Tensile crack coalescence pattern, (f, g) Mixed shear/tensile crack coalescence pattern, and (h) Other crack coalescence pattern (modified after Shen et al., 1995; Bobet, 1997; Bobet and Einstein, 1998).

5.2. Crack coalescence pattern

The interaction between pre-existing flaws and the crack initiation and propagation would lead to the coalescence phenomenon around the rock bridge. Based on previous studies, the crack coalescence pattern of the samples containing two parallel flaws can be classified into five types (Fig. 18): (1) no coalescence, (2) shear crack coalescence, (3) tensile crack coalescence, (4) mixed shear/tensile crack coalescence, and (5) other crack coalescence (Shen et al., 1995; Bobet and Einstein, 1998; Gonçalves Da Silva and Einstein, 2013). The no coalescence pattern reveals that this flaw geometry has little influence on crack interaction. The shear crack coalescence pattern results from secondary cracks, and the crack surface is rough and usually covered by pulverized powder (Fig. 19c). The wing cracks might be initiated in tension, and thus the crack surfaces in the tensile crack coalescence pattern are clean and smooth (Fig. 19a and b). When the crack surface has the characteristics of both shear and tensile crack coalescences, this pattern can be regarded as the mixed shear/tensile crack coalescence pattern (Fig. 19d and e).

Though observing crack surfaces can determine the cracking mechanism of pre-cracked rocks to a certain extent, the method validity has not been systematically confirmed. Furthermore, several samples may remain intact when they fail, making it hard to observe the crack surface (Reyes and Einstein, 1991). To solve this problem, the coalesced cracks were depicted using wing and secondary cracks (Bobet and Einstein, 1998; Park and Bobet, 2009). Wong and Chau (1998) utilized wing cracks to describe tensile cracks generated in sandstone, and they obtained nine types of crack coalescence patterns, including one of shear crack coalescence, two of mixed shear/wing tensile crack coalescence, three of wing tensile crack coalescence, and three of mixed wing tensile/wing tensile crack coalescence. Additionally, the nine types of crack coalescence patterns were determined by characterizing coalesced cracks with wing, coplanar secondary and oblique cracks (Sagong, 2001; Sagong and Bobet, 2002; Park, 2008; Park and Bobet, 2009). To accurately investigate the crack coalescence process, Wong (2008) and Wong and Einstein (2009a) utilized a high-speed camera to monitor the failure process and obtained nine types of crack coalescence patterns. Though some crack coalescence patterns have been identified in the past decades, the underlying mechanism of crack coalescence is not fully understood.

5.3. Influence of flaw geometry on crack coalescence pattern

5.3.1. Flaw inclination angle

Fig. 20 shows the crack coalescence patterns of samples containing two coplanar flaws with various flaw inclination angles. The flaw length and rock bridge length are both 12.7 mm. It can be found that the crack coalescence around the rock bridge is difficult to occur for samples with small flaw inclination angle α. With the increase in the inclination angle, the crack coalescence pattern changes as follows: no crack coalescence pattern → shear crack

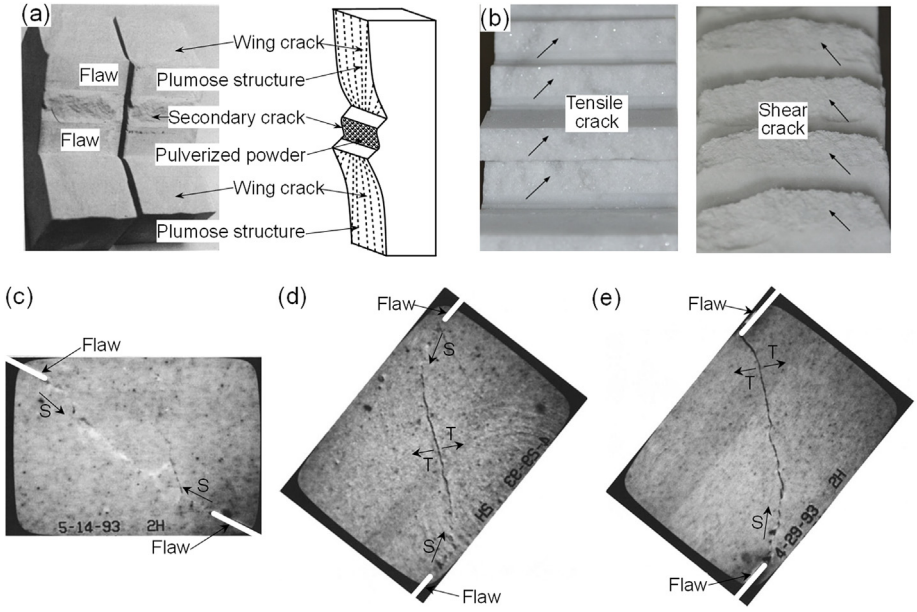

Fig. 19. Sample photos when cracks coalesce: (a) Crack surface characteristics, (b, c) Tensile and shear crack coalescence patterns, and (d, e) Mixed shear-tensile crack coalescence patterns, reproduced with permission from AGU (Shen, 1993, 1995; Shen et al., 1995; Bobet, 1997; Cheng et al., 2015).

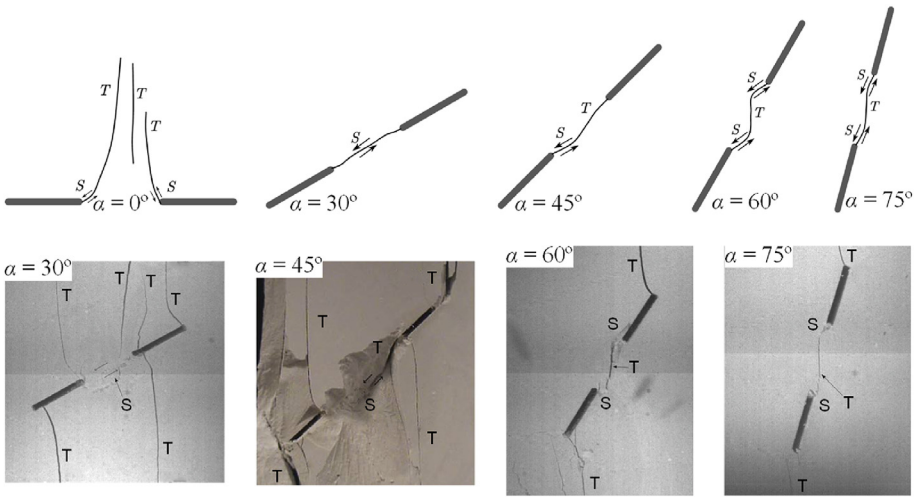

Fig. 20. Crack coalescence patterns of samples containing two coplanar flaws with different flaw inclination angles (modified after Wong, 2008; Wong and Einstein, 2009a).

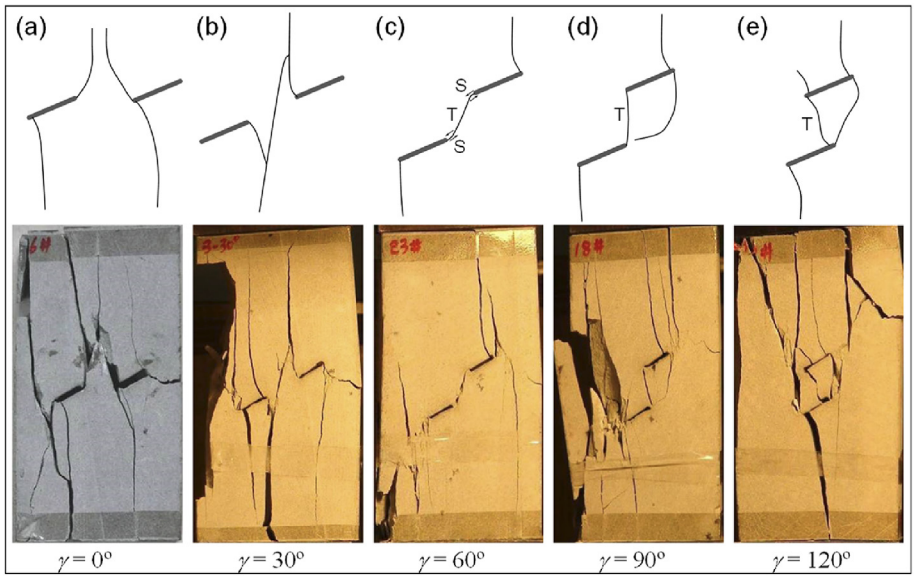

Fig. 21. Crack coalescence patterns of samples containing two parallel flaws with different rock bridge angles γ: (a) No coalescence pattern, (b) Indirect coalescence pattern, (c) Mixed shear/tensile crack coalescence pattern, and (d, e) Tensile crack coalescence pattern (Wong and Einstein, 2009a; Yang et al., 2016).

coalescence pattern → mixed shear/tensile crack coalescence pattern → tensile crack coalescence pattern (Wong, 2008; Wong and Einstein, 2009a; Morgan et al., 2013; Morgan and Einstein, 2017).

5.3.2. Rock bridge angle

Fig. 21 illustrates the crack coalescence patterns of samples with two parallel flaws, which have different rock bridge angles. When the rock bridge angle is small, the crack coalescence phenomenon is hard to appear around the rock bridge, which usually coalesces in an indirect pattern (Fig. 21a and b). With the increasing of rock bridge angle, the crack coalescence pattern changes from the shear crack coalescence to the mixed shear/tensile crack coalescence or tensile crack coalescence (Fig. 21c and e). In the shear crack coalescence pattern, cracks are usually initiated from the flaw tips and propagate towards the rock bridge center, while it is reverse in the mixed shear/tensile crack coalescence pattern (Shen, 1993; Shen et al., 1995). The coalescence stress in the shear crack coalescence pattern is usually greater than that in the mixed shear/tensile crack coalescence pattern, and the coalescence stress in the tensile crack coalescence pattern is the smallest (Park and Bobet, 2009).

5.3.3. Rock bridge length

Fig. 22 illustrates the crack coalescence pattern of samples containing two parallel flaws with different rock bridge lengths. It is widely accepted that the increase in rock bridge length L_r weakens the interaction between pre-existing flaws, which results in the crack coalescence pattern changing from direct crack coalescence to indirect crack coalescence, or indirect crack coalescence pattern to no crack coalescence (Fig. 22a and b). In terms of the effects of flaw inclination and rock bridge angles, the crack coalescence pattern has different variation tendencies as the rock bridge length L_r increases, e.g. the type II tensile crack coalescence pattern changes into a type VII shear crack coalescence pattern, and the type I tensile crack coalescence pattern changes into a type IV tensile crack coalescence pattern (Fig. 22c and d).

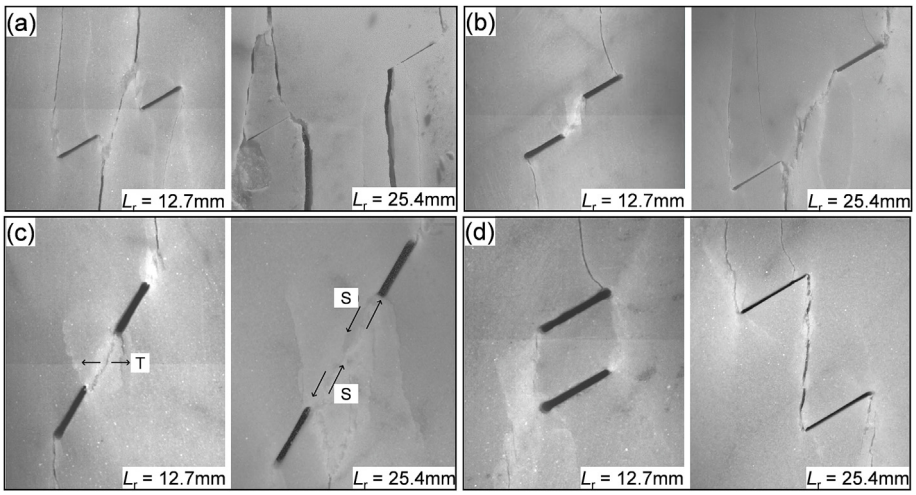

Fig. 22. Crack coalescence pattern changes of samples containing two parallel flaws with different lengths of rock bridge: (a) From indirect coalescence to no coalescence, (b) From direct coalescence to indirect coalescence, (c) From type II tensile crack coalescence to type VII shear crack coalescence, (d) From type I tensile crack coalescence to type IV tensile crack coalescence (types I, II, IV and VI are shown in Fig. 8b, reproduced with permission from MIT Libraries (Wong, 2008)).

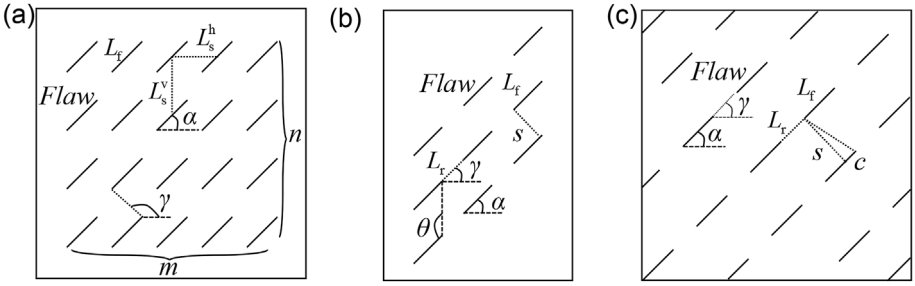

Fig. 23. Three types of samples containing multiple pre-existing flaws with different geometries in experiments: (a) Type a, (b) Type b, and (c) Type c (Sagong and Bobet, 2002; Prudencio and Van Sint Jan 2007; Cao et al., 2016; Yang et al., 2017b; Chen et al., 2018; Liu and Dai, 2021).

6. Mechanical characteristics and failure pattern of rocks containing multiple flaws

6.1. Geometry of pre-existing flaw

Samples containing multiple pre-existing flaws are related to jointed rocks in practical engineering (Lisjak and Grasselli, 2014). It is thus beneficial to investigate the mechanical characteristics and failure pattern of pre-cracked samples for understanding the engineering failure mechanism. As displayed in Fig. 23, the geometry of pre-existing flaws in experiments is usually depicted by some parameters, such as flaw inclination angle α, flaw length L_f, rock bridge length L_r and rock bridge angle γ. The samples containing multiple flaws with different geometries can be classified into 3 types, i.e. Type a, Type b, and Type c. The flaw inclination angle is equal to the rock bridge angle in Types a and b samples, while it is different in Type c samples. Table 4 summarizes the geometrical characteristics of samples containing multiple flaws in experiments.

6.2. Mechanical characteristics of samples containing multiple flaws

The normalized peak strength of samples containing multiple flaws increases with the increasing flaw inclination angle (Fig. 24). When the number of flaws n increases or the spacing s decreases, the total flaw number in samples accordingly decreases, and the normalized peak strength presents an increasing trend. When the inclination angle is small, the increasing magnitude of normalized peak strength is large. As the inclination angle increases, the increasing magnitude of normalized peak strength gradually becomes inconspicuous (Fig. 24a and c). When the continuity c increases, the normalized peak strength presents an increasing tendency (Fig. 24d). Based on the displacement distribution on sample surfaces, Yang et al. (2017b) found the maximum value of displacement decreases with respect to the spacing, resulting in the general decrease of normalized peak strength.

6.3. Failure pattern of samples containing multiple flaws

As presented in Fig. 25, Prudencio and Van Sint Jan (2007) found three types of failure patterns for samples containing multiple flaws, including (A) failure pattern through a plane, (B) failure pattern induced by the rotation of new blocks, and (C) stepped failure pattern (Fig. 25b and c). In Type A, crack initiation occurs in the same set of coplanar flaws. The propagation path of cracks is along the direction of the rock bridge, and the inclination angle of failure surfaces is approximately equal. In Type B, the crack initiation and propagation from the tips of non-coplanar flaws result in the formation of new blocks, and the rotation of these blocks induces the sample failure. In the stepped failure pattern, the sliding of flaws leads to the initiation and propagation of wing cracks, and then the wing crack coalescence results in material failure. Sagong and Bobet (2002) summarized four types of failure patterns for samples containing multiple flaws, the Type D failure pattern looks like the stepped failure pattern. Apart from the Type A failure pattern, the crack coalescences in other three failure patterns

Table 4
Summary of the geometrical characteristics of samples containing multiple pre-existing flaws in experiments.

Material	Length × width × height (mm × mm × mm)	Geometry type	Geometrical parameter	Source
Rock-like material	200 × 150 × 30	Type a	$L_f = 20$ mm, $L_s^h = 30$ mm, $\alpha = 25°, 45°, 75°, 90°$, γ = w/o, $m = 5$, $n = 1–4$@1 $L_s^v = 40, 50, 100$ mm	Cao et al. (2016)
Rock-like material	150 × 90 × 70	Type a	$L_f = 20$ mm, $\alpha = 60°$, γ = w/o, $m = n = 3$ $L_s^h = 15$ mm, $L_s^v = 38, 48$ mm	Zhou et al. (2018)
Rock-like material	200 × 150 × 30	Type a	$L_f = 20$ mm, $L_s^h = 30$ mm, $\alpha = 25°, 45°, 75°, 90°$ γ = w/o, $m = 5$, $n = 3–6$@1, $L_s^v = 30, 40, 50$ mm	Pu and Cao (2012)
Rock-like material	300 × 150 × 50	Type b	$L_f = 25, 50$ mm, $L_r = 10, 20, 30$ mm, $s = 10, 20, 40$ mm $\alpha = \gamma = 30°–75°$@15°, θ = w/o	Prudencio and Van Sint Jan (2007)
Rock-like material	200 × 100 × 100	Type b	$L_f = L_r = 15$ mm, $s = 18$ mm $\alpha = \gamma = 45°$, $\theta = 135°$	Feng et al. (2018)
Rock-like material	200 × 100 × 100	Type b	$L_f = 15$ mm, $L_r = 20$ mm, $s = 24$ mm $\alpha = \gamma = 45°$, $\theta = 135°$	Liu et al. (2018a, b)
Gypsum	160 × 80 × 50	Type b	$L_f = 12$ mm, $2b = 10$ mm, $s = 10$ mm $\theta = 90° + \alpha$, $\alpha = \gamma = 0°–90°$@15°	Chen et al. (2018)
Mortar	200 × 150 × 150	Type b	$L_f = 25–40$ mm@5 mm, $L_r = 45$ mm $s = 30–60$ mm@10 mm $\theta = 90° + \alpha$, $\alpha = \gamma = 30°, 45°, 60°, 90°$	Huang et al. (2019)
Gypsum	203.2 × 101.6 × 30	Type c	$L_f = 2a = L_r = 12.7$ mm, $s = a–2a$@a $c = -2a–2a$@a, $\alpha = \gamma = 30°–60°$@15°	Sagong and Bobet (2002)
Gypsum	150 × 150 × 50	Type c	$L_f = 18$ mm, $L_r = 12$ mm, $\alpha = \gamma = 0°–90°$@15° $s = 30, 37.5, 50, 75$ mm, $c = 3, 10.5, 18$ mm	Yang et al. (2017b)
Gypsum	150 × 150 × 50	Type c	$L_f = L_r$ = w/o, $\alpha = \gamma = 0°–90°$@15° $s = 30$ mm, c = w/o	Chen et al. (2012, 2014)
Gypsum	150 × 150 × 50	Type c	$L_f = c = 0–24$ mm@6 mm, L_r = w/o, $\alpha = \gamma = 0°–90°$@15°, $s = 30$ mm	Chen et al. (2013)

Note: The geometry type is consistent with that in Fig. 23. The number after @ is the increment; θ is the flaw tip-to-tip angle; s is the spacing; c is the continuity; L_s^h and L_s^v are the distances along the horizontal and vertical directions, respectively; m and n are the numbers of flaws along the horizontal and vertical directions, respectively.

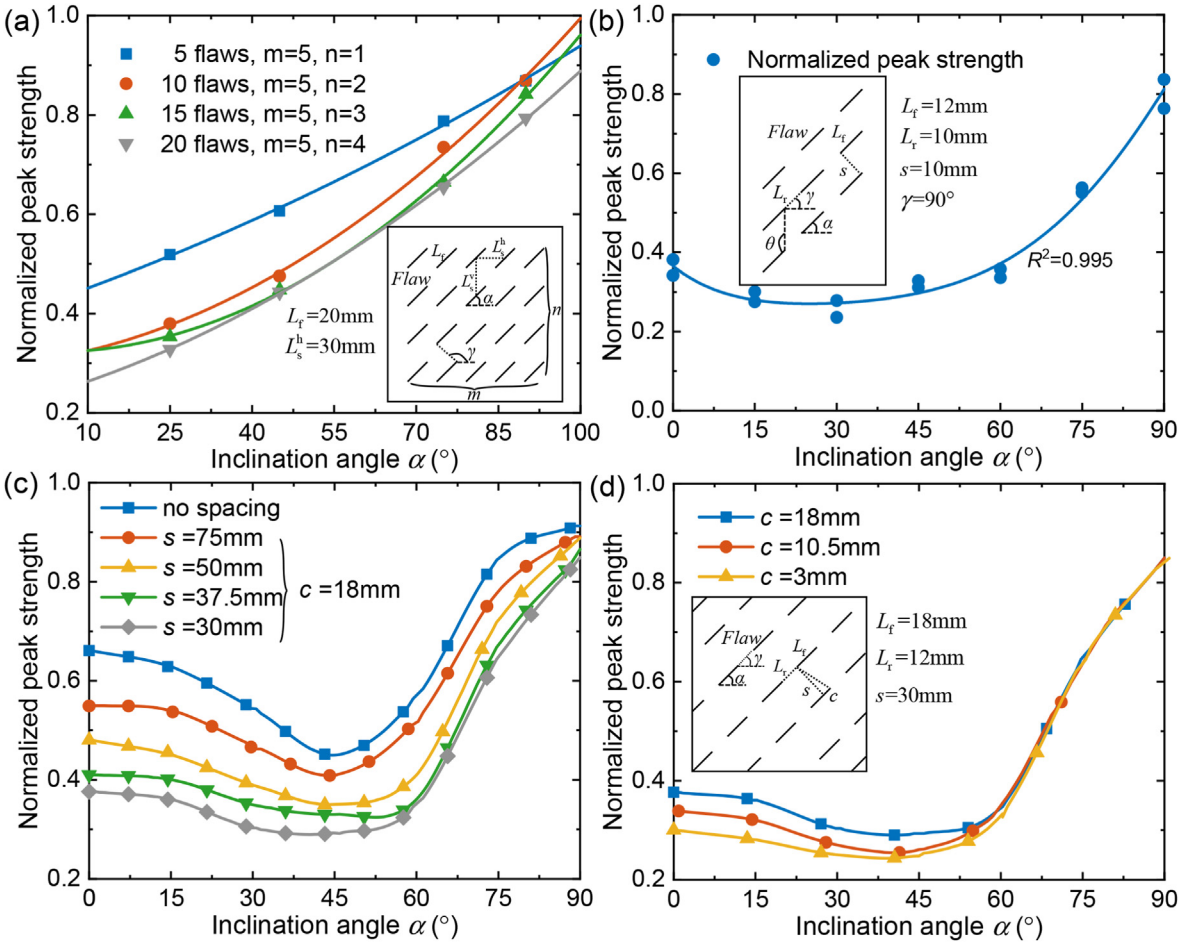

Fig. 24. Effect of flaw inclination angle on normalized peak strength of samples containing multiple flaws with different geometrical characteristics: (a) The geometry type is Type a, (b) The geometry type is Type b, and (c, d) The geometry type is Type c (data from Cao et al., 2016; Yang et al., 2017b; Chen et al., 2018). No spacing means one set of pre-existing flaws existing in sample.

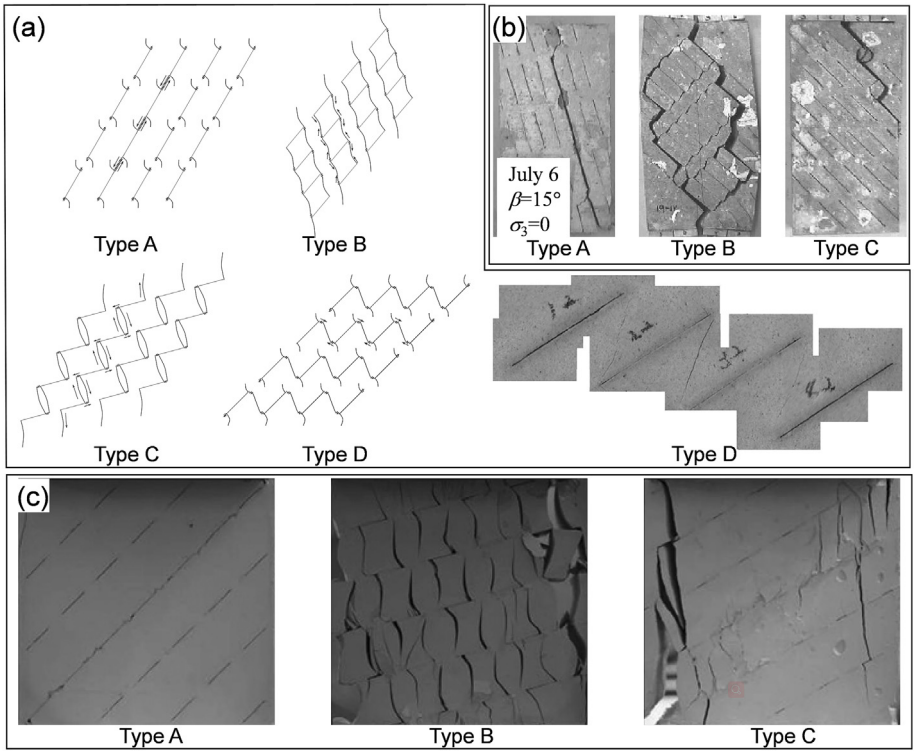

Fig. 25. Failure patterns of samples with multiple flaws: (a) Sketches of failed samples, and (b, c) Photos of failed samples (reproduced from Sagong and Bobet, 2002; Prudencio and Van Sint Jan 2007; Chen et al., 2013). Type A is the failure pattern through a plane, Type B is the failure pattern induced by rotation of new blocks, and Type C is the stepped failure pattern.

occur around the rock bridge in a "columnar" manner, and the linkage of the non-coplanar pre-existing flaws leads to sample failure. To reveal the cracking mechanism, many researchers divided the failure patterns into tensile, shear, and mixed tensile/shear failure patterns (Cao et al., 2016; Yang et al., 2017b; Chen et al., 2018).

7. Conclusions

The failure of rock materials under compression is related to the crack initiation, propagation and coalescence processes. This review introduces the brittle deformation and crack stress level of intact samples, revealing that the material failure is associated with microcrack growth. Then a series of nondestructive techniques utilized in experiments, including AE, ultrasonic technique, X-ray CT, DIC and digital photoelastic technique, is presented. The mechanical characteristics and cracking processes obtained from samples containing one, two and multiple flaws are reviewed as well. The following conclusions can be drawn:

(1) In the case of samples containing one pre-existing flaw, different crack initiation patterns are obtained. Based on the crack initiation sequence and geometrical characteristics, three crack initiation patterns, including wing crack, coplanar secondary crack, and oblique secondary crack, are determined. Utilizing a high-speed camera to monitor cracking processes, twelve types of crack initiation patterns related to different cracking mechanisms are identified, i.e. five of tensile cracks, three of shear cracks, one of mixed tensile/shear crack, one of lateral crack, one of far-field crack, and one of surface spalling crack.

(2) As to samples containing one single flaw, the pre-existing flaw significantly degrades the mechanical characteristics of rocks. When the flaw length increases, mechanical properties present decreasing trends. When the flaw width decreases, open flaw gradually becomes a closed one. The crack initiation patterns are similar in samples containing open and closed flaws. As the flaw inclination angle increases, mechanical properties generally increase, while the crack initiation angle presents a decreasing tendency. The crack initiation patterns identified in biaxial compression tests are similar with the results in uniaxial compression tests. As the confining pressure increases, cracks become more difficult to initiate. Concerning samples containing flaws filled by different minerals, normalized peak strength and initiation stress generally increase with increasing inclination angle, while the initiation angle has a converse variation trend.

(3) In terms of samples containing two pre-existing flaws, the flaw geometry can be divided into two types, i.e. parallel and unparallel flaws. As to samples containing parallel flaws, the effect of increasing inclination angle on crack coalescence pattern is presented as follows: no crack coalescence → shear crack coalescence → mixed shear/tensile crack coalescence → tensile crack coalescence. As the rock bridge angle increases, the crack coalescence pattern generally changes from the shear crack coalescence to the mixed shear/tensile crack coalescence or the tensile crack coalescence. The interaction between pre-existing flaws is weakened with increasing rock bridge length, and the crack coalescence pattern changes from a direct crack coalescence to an indirect crack coalescence or from an indirect crack coalescence to no crack coalescence.

(4) The samples containing multiple pre-existing flaws can be summarized into three types. As flaw inclination angle increases or number of flaws and continuity decreases, normalized peak strength generally presents an increasing

tendency. Based on the geometry of stress-induced cracks in samples containing multiple flaws, several types of failure patterns, including the failure pattern through a plane, the failure pattern induced by rotation of new blocks, and the stepped failure pattern, are summarized.

Declaration of competing interest

The authors declare that they have no known competing financial interests or personal relationships that could have appeared to influence the work reported in this paper.

Acknowledgments

We gratefully acknowledge the financial support from the National Key R&D Program of China (Grant No. 2020YFA0711802). The authors acknowledge the constructive comments from the anonymous reviewers and the editor. Besides, Dr. Yanlong Zheng from Southeast University is sincerely acknowledged for his help in improving the paper's quality. The authors are also grateful for the permissions from Springer, Elsevier, MIT Libraries, and ARMA.

Appendix A. Supplementary data

Supplementary data to this article can be found online at https://doi.org/10.1016/j.jrmge.2022.03.013.

References

Abaab, N., Zanella, A., Akrout, D., Mourgues, R., Montacer, M., 2021. Timing and distribution of bedding-parallel veins, in evaporitic rocks, Bouhedma Formation, Northern Chotts, Tunisia. J. Struct. Geol. 153, 104461.
Adachi, J., Siebrits, E., Peirce, A., Desroches, J., 2007. Computer simulation of hydraulic fractures. Int. J. Rock Mech. Min. Sci. 44, 739–757.
Ajovalasit, A., Barone, S., Petrucci, G., 1998. A review of automated methods for the collection and analysis of photoelastic data. J. Strain Anal. Eng. Des. 33, 75–91.
Ajovalasit, A., Pitarresi, G., Zuccarello, B., 2007. Limitation of carrier fringe methods in digital photoelasticity. Opt Laser. Eng. 45, 631–636.
Aliabadian, Z., Sharafisafa, M., Tahmasebinia, F., Shen, L., 2021. Experimental and numerical investigations on crack development in 3D printed rock-like specimens with pre-existing flaws. Eng. Fract. Mech. 241, 107396.
Barone, S., Burriesci, G., Petrucci, G., 2002. Computer aided photoelasticity by an optimum phase stepping method. Exp. Mech. 42, 132–139.
Baxter, M.G., Pullin, R., Holford, K.M., Evans, S.L., 2007. Delta T source location for acoustic emission. Mech. Syst. Signal Process. 21, 1512–1520.
Bieniawski, Z.T., 1967. Mechanism of brittle fracture of rock. Part II-experimental studies. Int. J. Rock Mech. Min. Sci. 4, 407–423.
Blaber, J., Adair, B., Antoniou, A., 2015. Ncorr: open-source 2D digital image correlation Matlab software. Exp. Mech. 55, 1105–1122.
Bobet, A., 1997. Fracture Coalescence in Rock Materials: Experimental Observations and Numerical Predictions. PhD Thesis. Massachusetts Institute of Technology, Cambridge, MA, USA.
Bobet, A., Einstein, H.H., 1998. Fracture coalescence in rock-type materials under uniaxial and biaxial compression. Int. J. Rock Mech. Min. Sci. 35, 863–888.
Bobet, A., 2000. The initiation of secondary cracks in compression. Eng. Fract. Mech. 66, 187–219.
Bombolakis, E.G., 1968. Photoelastic study of initial stages of brittle fracture in compression. Tectonophysics (6), 461–473.
Brace, W.F., Bombolakis, E.G., 1963. A note on brittle crack growth in compression. J. Geophys. Res. 68, 3709–3713.
Brace, W.F., Paulding, B.W., Scholz, C., 1966. Dilatancy in the fracture of crystalline rocks. J. Geophys. Res. 71, 3939–3953.
Brideau, M.A., Yan, M., Stead, D., 2009. The role of tectonic damage and brittle rock fracture in the development of large rock slope failures. Geomorphology 103, 30–49.
Brooks, Z., Ulm, F.J., Einstein, H.H., 2013. Environmental scanning electron microscopy (ESEM) and nanoindentation investigation of the crack tip process zone in marble. Acta Geotech. (8), 223–245.
Cai, M., Kaiser, P.K., Tasaka, Y., et al., 2004. Generalized crack initiation and crack damage stress thresholds of brittle rock masses near underground excavations. Int. J. Rock Mech. Min. Sci. 41, 833–847.
Cao, P., Liu, T., Pu, C., Lin, H., 2015. Crack propagation and coalescence of brittle rock-like specimens with pre-existing cracks in compression. Eng. Geol. 187, 113–121.
Cao, R. hong, Cao, P., Lin, H., Pu, C. zhi, Ou, K., 2016. Mechanical behavior of brittle rock-like specimens with pre-existing fissures under uniaxial loading: experimental studies and particle mechanics approach. Rock Mech. Rock Eng. 49, 763–783.
Cao, R., Cao, P., Lin, H., et al., 2019. Crack initiation, propagation, and failure characteristics of jointed rock or rock-like specimens: a review. Adv. Civ. Eng. 2019, 1–31.
Cao, R., Yao, R., Meng, J., et al., 2020. Failure mechanism of non-persistent jointed rock-like specimens under uniaxial loading: laboratory testing. Int. J. Rock Mech. Min. Sci. 132, 104341.
Chang, X., Deng, Y., Li, Z., Wang, S., Tang, C.A., 2018. Crack propagation from a filled flaw in rocks considering the infill influences. J. Appl. Geophys. (152), 137–149.
Chen, X., Wang, S., Li, L., 2012. Characteristics of fragments of jointed rock mass model under uniaxial compression. Yanshilixue Yu Gongcheng Xuebao/Chinese J. Rock Mech. Eng. 31, 898–907.
Chen, X., Liao, Z.H., Peng, X., 2013. Cracking process of rock mass models under uniaxial compression. J. Cent. South Univ. 20, 1661–1678.
Chen, X., Lu, W., Sun, J., 2014. Damage evolution of jointed rock masses under uniaxial compression based on digital image analysis. Yanshilixue Yu Gongcheng Xuebao/Chinese J. Rock Mech. Eng. 33, 1149–1157.
Chen, M., Yang, S., Pathegama Gamage, R., et al., 2018. Fracture processes of rock-like specimens containing nonpersistent fissures under uniaxial compression. Energies 12, 79.
Cheng, Y., Wong, L.N.Y., Zou, C., 2015. Experimental study on the formation of faults from en-echelon fractures in Carrara Marble. Eng. Geol. 195, 312–326.
Cnudde, V., Boone, M.N., 2013. High-resolution X-ray computed tomography in geosciences: a review of the current technology and applications. Earth Sci. Rev. 123, 1–17.
de Joussineau, G., Petit, J.P., Gauthier, B.D.M., 2003. Photoelastic and numerical investigation of stress distributions around fault models under biaxial compressive loading conditions. Tectonophysics 363, 19–43.
del Viso, J.R., Carmona, J.R., Ruiz, G., 2008. Shape and size effects on the compressive strength of high-strength concrete. Cement Concr. Res. 38, 386–395.
Dong, Y.L., Pan, B., 2017. A review of speckle pattern fabrication and assessment for digital image correlation. Exp. Mech. 57, 1161–1181.
Dong, Q.Q., Wei, H.J., Ma, G.W., 2020. Failure mechanism of S-shaped fissure in brittle materials under uniaxial tension: experimental and numerical analyses. Int. J. Solid Struct. 191–192, 486–496.
Dontsov, E.V., Peirce, A.P., 2015. Proppant transport in hydraulic fracturing: crack tip screen-out in KGD and P3D models. Int. J. Solid Struct. 63, 206–218.
Duan, Y., Li, X., Zheng, B., He, J., Hao, J., 2019. Cracking evolution and failure characteristics of Longmaxi shale under uniaxial compression using real-time computed tomography scanning. Rock Mech. Rock Eng. 52, 3003–3015.
Dyskin, A.V., Sahouryeh, E., Jewell, R.J., Joer, H., Ustinov, K.B., 2003. Influence of shape and locations of initial 3-D cracks on their growth in uniaxial compression. Eng. Fract. Mech. 70, 2115–2136.
Eberhardt, E., Stead, D., Stimpson, B., Read, R.S., 1997. Changes in acoustic event properties with progressive fracture damage. Int. J. Rock Mech. Min. Sci. 34, 71.e1–71.e12.
Eberhardt, E., Stead, D., Stimpson, B., Read, R.S., 1998. Identifying crack initiation and propagation thresholds in brittle rock. Can. Geotech. J. 35, 222–233.
Esterhuizen, G.S., Dolinar, D.R., Ellenberger, J.L., 2011. Pillar strength in underground stone mines in the United States. Int. J. Rock Mech. Min. Sci. 48, 42–50.
Euser, B., Rougier, E., Lei, Z., et al., 2019. Simulation of fracture coalescence in granite via the combined finite–discrete element method. Rock Mech. Rock Eng. 52, 3213–3227.
Feldkamp, L.A., Davis, L.C., Kress, J.W., 1984. Practical cone-beam algorithm. J. Opt. Soc. Am. A 1, 612–619.
Feng, X.T., Ding, W., Zhang, D., 2009. Multi-crack interaction in limestone subject to stress and flow of chemical solutions. Int. J. Rock Mech. Min. Sci. 46, 159–171.
Feng, P., Dai, F., Liu, Y., Xu, N., Zhao, T., 2018. Effects of strain rate on the mechanical and fracturing behaviors of rock-like specimens containing two unparallel fissures under uniaxial compression. Soil Dynam. Earthq. Eng. 110, 195–211.
Feng, P., Dai, F., Liu, Y., Xu, N., wen, Du, bo, H., 2019. Coupled effects of static-dynamic strain rates on the mechanical and fracturing behaviors of rock-like specimens containing two unparallel fissures. Eng. Fract. Mech. 207, 237–253.
Flannery, B.P., Deckman, H.W., Roberge, W.G., D'Amico, K.L., 1987. Three-dimensional X-ray microtomography. Science (80-.) 237, 1439–1444.
Fortin, J., Stanchits, S., Dresen, G., Guéguen, Y., 2006. Acoustic emission and velocities associated with the formation of compaction bands in sandstone. J. Geophys. Res. Solid Earth 111, 1–16.
Fu, J.W., Liu, S.L., Zhu, W.S., Zhou, H., Sun, Z. chuan, 2018. Experiments on failure process of new rock-like specimens with two internal cracks under biaxial loading and the 3-D simulation. Acta Geotech. 13, 853–867.
Garg, P., Shirole, D., Hedayat, A., Griffiths, D.V., 2019. Coupled ultrasonic and digital imaging of crack initiation and growth in prismatic Lyon sandstone rocks. 53rd US Rock Mech Symp.
Gautam, P.K., Verma, A.K., Jha, M.K., Sharma, P., Singh, T.N., 2018. Effect of high temperature on physical and mechanical properties of Jalore granite. J. Appl. Geophys. 159, 460–474.
Geoff Tanner, P.W., 2016. A new model for the formation of a spaced crenulation (shear band) cleavage in the Dalradian rocks of the Tay Nappe, SW Highlands, Scotland. J. Struct. Geol. 84, 120–141.
Giachetti, A., 2000. Matching techniques to compute image motion. Image Vis Comput. 18, 247–260.
Glover, P.W.J., Baud, P., Darot, M., et al., 1995. A/B phase transition in quartz monitored using acoustic emissions. Geophys. J. Int. 120, 775–782.

Gonçalves Da Silva, B., Einstein, H.H., 2013. Modeling of crack initiation, propagation and coalescence in rocks. Int. J. Fract. 182, 167–186.
Gonçalves da Silva, B., Einstein, H., 2018. Physical processes involved in the laboratory hydraulic fracturing of granite: visual observations and interpretation. Eng. Fract. Mech. 191, 125–142.
Gong, C.G., Wang, W., Shao, J.F., Wang, R. Bin, Feng, X.W., 2021. Effect of water chemical corrosion on mechanical properties and failure modes of pre-fissured sandstone under uniaxial compression. Acta Geotech. 16, 1083–1099.
Graham, C.C., Stanchits, S., Main, I.G., Dresen, G., 2010. Comparison of polarity and moment tensor inversion methods for source analysis of acoustic emission data. Int. J. Rock Mech. Min. Sci. 47, 161–169.
Grün, A., 1985. Adaptive least-squares correlation: a powerful image matching technique. South Afr. J. Photogrammetry, Remote Sens. Cartogr. 14, 175–187.
Gunarathna, G., Gonçalves da Silva, B., 2021. Effect of the triaxial state of stress in the hydraulic fracturing processes of granite: Part 1—Visual observations and interpretation. Rock Mech. Rock Eng. 54, 2903–2923.
Güneş Yilmaz, N., Mete Goktan, R., Kibici, Y., 2011. Relations between some quantitative petrographic characteristics and mechanical strength properties of granitic building stones. Int. J. Rock Mech. Min. Sci. 48, 506–513.
Hall, S.A., de Sanctis, F., Viggiani, G., 2006. Monitoring fracture propagation in a soft rock (Neapolitan Tuff) using acoustic emissions and digital images. Pure Appl. Geophys. 163, 2171–2204.
Hall, S.A., Bornert, M., Desrues, J., et al., 2010. Discrete and continuum analysis of localised deformation in sand using X-ray μCT and volumetric digital image correlation. Geotechnique 60, 315–322.
Han, T., Wang, X., Li, D., et al., 2019. Damage and degradation mechanism for single intermittent cracked mortar specimens under a combination of chemical solutions and dry-wet cycles. Construct. Build. Mater. 213, 567–581.
Henley, R.W., Ellis, A.J., 1983. Geothermal systems ancient and modern: a geochemical review. Earth Sci. Rev. 19, 1–50.
Heuze, F.E., 1983. High-temperature mechanical, physical and Thermal properties of granitic rocks- A review. Int. J. Rock Mech. Min. Sci. 20, 3–10.
Hoek, E., Franklin, J.A., 1968. A simple triaxial cell for field and laboratory testing of rock. Trans. Inst. Min. Metall. 77, 22–26.
Hoek, E., Bieniawski, Z.T., 1984. Brittle fracture propagation in rock under compression. Int. J. Fract. 26, 276–294.
Homand-Etienne, F., Houpert, R., 1989. Thermally induced microcracking in granites: characterization and analysis. Int. J. Rock Mech. Min. Sci. 26, 125–134.
Horii, H., Nemat-Nasser, S., 1985. Compression-induced microcrack growth in brittle solids: axial splitting and shear failure. J. Geophys. Res. 90, 3105–3125.
Horii, H., Trans, P., Lond, R.S., 1986. Brittle failure in compression: splitting faulting and brittle-ductile transition. Philos. Trans. R. Soc. London. Ser. A, Math. Phys. Sci. 319, 337–374.
Huang, J., Ganglin, C., Yonghong, Z., Ren, W., 1990. An experimental study of the strain field development prior to failure of a marble plate under compression. Tectonophysics 175, 269–284.
Huang, C., Yang, W., Duan, K., et al., 2019. Mechanical behaviors of the brittle rock-like specimens with multi-non-persistent joints under uniaxial compression. Construct. Build. Mater. 220, 426–443.
Huang, D., Yan, Z., Zhong, Z., et al., 2021. Experimental study on failure behaviour of ligaments between strike-inconsistent fissure pairs under uniaxial compression. Rock Mech. Rock Eng. 54, 1257–1275.
Ishida, T., Labuz, J.F., Manthei, G., et al., 2017. ISRM suggested method for laboratory acoustic emission monitoring. Rock Mech. Rock Eng. 50, 665–674.
Jiang, C., Zhao, G.F., 2015. A preliminary study of 3D printing on rock mechanics. Rock Mech. Rock Eng. 48, 1041–1050.
Jin, J., Cao, P., Chen, Y., et al., 2017. Influence of single flaw on the failure process and energy mechanics of rock-like material. Comput. Geotech. 86, 150–162.
Johns, R.A., Steude, J.S., Castanier, L.M., Roberts, P.V., 1993. Nondestructive measurements of fracture aperture in crystalline rock cores using X ray computed tomography. J. Geophys. Res. 98, 1889–1900.
Ju, Y., Ren, Z., Wang, L., Mao, L., Chiang, F.P., 2018. Photoelastic method to quantitatively visualise the evolution of whole-field stress in 3D printed models subject to continuous loading processes. Opt Laser. Eng. 100, 1339–1351.
Ju, Y., Ren, Z., Li, X., et al., 2019. Quantification of hidden whole-field stress inside porous geomaterials via three-dimensional printing and photoelastic testing methods. J. Geophys. Res. Solid Earth 124, 5408–5426.
Ju, Y., Wang, Y., Ren, Z., et al., 2020. Optical method to quantify the evolution of whole-field stress in fractured coal subjected to uniaxial compressive loads. Opt Laser. Eng. 128, 106013.
Ju, Y., Liu, P., Ren, Z., Mao, L., Chiang, F., 2021. Characterization of stress field evolution during 3D internal fracture propagation using additively printed models and frozen stress techniques. Theor. Appl. Fract. Mech. 111, 102870.
Kammers, A.D., Daly, S., 2013. Digital image correlation under scanning electron microscopy: methodology and validation. Exp. Mech. 53, 1743–1761.
Ketcham, R.A., Carlson, W.D., 2001. Acquisition, optimization and interpretation of x-ray computed tomographic imagery: applications to the geosciences. Comput. Geosci. 27, 381–400.
Ketcham, R.A., 2005. Three-dimensional grain fabric measurements using high-resolution X-ray computed tomography. J. Struct. Geol. 27, 1217–1228.
Kou, M., Liu, X., Tang, S., Wang, Y., 2019. 3-D X-ray computed tomography on failure characteristics of rock-like materials under coupled hydro-mechanical loading. Theor. Appl. Fract. Mech. 104, 102396.
Kovalyshen, Y., Detournay, E., 2010. A reexamination of the classical PKN model of hydraulic fracture. Transport Porous Media 81, 317–339.
Kundu, T., 2014. Acoustic source localization. Ultrasonics 54, 25–38.
Lajtai, E.Z., 1971. A theoretical and experimental evaluation of the Griffith theory of brittle fracture. Tectonophysics 11, 129–156.
Lajtai, E.Z., 1974. Brittle fracture in compression. Int. J. Fract. 10, 525–536.
Le, H., Sun, S., Kulatilake, P.H.S.W., Wei, J., 2018. Effect of grout on mechanical properties and cracking behavior of rock-like specimens containing a single flaw under uniaxial compression. Int. J. GeoMech. 18, 04018129.
Lecompte, D., Smits, A., Bossuyt, S., et al., 2006. Quality assessment of speckle patterns for digital image correlation. Opt Laser. Eng. 44, 1132–1145.
Lee, S., Ravichandran, G., 2003. An investigation of cracking in brittle solids under dynamic compression using photoelasticity. Opt Laser. Eng. 40, 341–352.
Lee, H., Jeon, S., 2011. An experimental and numerical study of fracture coalescence in pre-cracked specimens under uniaxial compression. Int. J. Solid Struct. 48, 979–999.
Lei, R., Zhang, Z., Berto, F., Ranjith, P.G., Liu, L., 2020. Cracking process and acoustic emission characteristics of sandstone with two parallel filled-flaws under biaxial compression. Eng. Fract. Mech. 237, 107253.
Levi, T., Avni, Y., Bahat, D., 2019. Evolution of the stress field near the Arava basin located along the Dead Sea Fault system as revealed by joint sets. J. Struct. Geol. 128, 103876.
Li, B.Q., Einstein, H.H., 2019. Direct and microseismic observations of hydraulic fracturing in barre granite and opalinus clayshale. J. Geophys. Res. Solid Earth 124, 11900–11916.
Li, H., Wong, L.N.Y., 2012. Influence of flaw inclination angle and loading condition on crack initiation and propagation. Int. J. Solids Struct. 49, 2482–2499.
Li, Y.P., Chen, L.Z., Wang, Y.H., 2005. Experimental research on pre-cracked marble under compression. Int. J. Solid Struct. 42, 2505–2516.
Li, Q., Xing, H., Liu, J., Liu, X., 2015. A review on hydraulic fracturing of unconventional reservoir. Petroleum 1, 8–15.
Li, B.Q., Gonçalves da Silva, B., Einstein, H., 2019a. Laboratory hydraulic fracturing of granite: acoustic emission observations and interpretation. Eng. Fract. Mech. 209, 200–220.
Li, D., Wang, E., Kong, X., Ali, M., Wang, D., 2019b. Mechanical behaviors and acoustic emission fractal characteristics of coal specimens with a pre-existing flaw of various inclinations under uniaxial compression. Int. J. Rock Mech. Min. Sci. 116, 38–51.
Li, H., Shen, R., Li, D., et al., 2019c. Acoustic emission multi-parameter analysis of dry and saturated sandstone with cracks under uniaxial compression. Energies 12, 1959.
Li, S., Zhang, D., Bai, X., et al., 2019d. Experimental study on mechanical properties, acoustic emission energies and failure modes of pre-cracked rock materials under uniaxial compression. Pure Appl. Geophys. 176, 4519–4532.
Li, X.F., Li, H.B., Liu, L.W., et al., 2020. Investigating the crack initiation and propagation mechanism in brittle rocks using grain-based finite-discrete element method. Int. J. Rock Mech. Min. Sci. 127, 104219.
Lin, H., Yang, H., Wang, Y., Zhao, Y., Cao, R., 2019a. Determination of the stress field and crack initiation angle of an open flaw tip under uniaxial compression. Theor. Appl. Fract. Mech. 104, 102358.
Lin, H., Yang, H., Wang, Y., Zhao, Y., Cao, R., 2019b. Determination of the stress field and crack initiation angle of an open flaw tip under uniaxial compression. Theor. Appl. Fract. Mech. 104, 102358.
Lin, Q., Cao, P., Liu, Y., Cao, R., Li, J., 2021. Mechanical behaviour of a jointed rock mass with a circular hole under compression-shear loading: experimental and numerical studies. Theor. Appl. Fract. Mech. 114, 102998.
Lisjak, A., Grasselli, G., 2014. A review of discrete modeling techniques for fracturing processes in discontinuous rock masses. J. Rock Mech. Geotech. Eng. 6, 301–314.
Liu, X., Liu, Q., Huang, S., Wei, L., Lei, G., 2016. Fracture propagation characteristic and micromechanism of rock-like specimens under uniaxial and biaxial compression. Shock Vib. 2016, 1–11.
Liu, Y., Dai, F., Fan, P., Xu, N., Dong, L., 2017. Experimental investigation of the influence of joint geometric configurations on the mechanical properties of intermittent jointed rock models under cyclic uniaxial compression. Rock Mech. Rock Eng. 50, 1453–1471.
Liu, Y., Dai, F., Dong, L., Xu, N., Feng, P., 2018a. Experimental investigation on the fatigue mechanical properties of intermittently jointed rock models under cyclic uniaxial compression with different loading parameters. Rock Mech. Rock Eng. 51, 47–68.
Liu, Y., Dai, F., Feng, P., Xu, N.W., 2018b. Mechanical behavior of intermittent jointed rocks under random cyclic compression with different loading parameters. Soil Dynam. Earthq. Eng. 113, 12–24.
Liu, X., Liu, Q., Liu, B., Zhu, Y., Zhang, P., 2019. Failure behavior for rocklike material with cross crack under biaxial compression. J. Mater. Civ. Eng. 31, 06018025.
Liu, L., Li, H., Li, X., Wu, R., 2020a. Full-field strain evolution and characteristic stress levels of rocks containing a single pre-existing flaw under uniaxial compression. Bull. Eng. Geol. Environ. 79, 3145–3161.
Liu, P., Ju, Y., Fu, G., Ren, Z., 2020b. Visualization of full-field stress evolution during 3D penetrated crack propagation through 3D printing and frozen stress techniques. Eng. Fract. Mech. 236, 107222.
Liu, L., Li, H., Chen, S., et al., 2021a. Effects of bedding planes on mechanical characteristics and crack evolution of rocks containing a single pre-existing flaw. Eng. Geol. 293, 106325.
Liu, L., Li, H., Li, X., Wu, D., Zhang, G., 2021b. Underlying mechanisms of crack initiation for granitic rocks containing a single pre-existing flaw: insights from digital image correlation (DIC) analysis. Rock Mech. Rock Eng. 54, 857–873.

Liu, Y., Dai, F., 2021. A review of experimental and theoretical research on the deformation and failure behavior of rocks subjected to cyclic loading. J. Rock Mech. Geotech. Eng. 13, 1203–1230.
Lockner, D., 1993. The role of acoustic emission in the study of rock fracture. Int. J. Rock Mech. Min. Sci. 30, 883–899.
Lu, Y., Wang, L., Elsworth, D., 2015. Uniaxial strength and failure in sandstone containing a pre-existing 3-D surface flaw. Int. J. Fract. 194, 59–79.
Lu, Y., Pu, H., Wang, L., et al., 2021. Fracture evolution in mudstone specimens containing a pre-existing flaw under true triaxial compression. Int. J. Rock Mech. Min. Sci. 138, 104594.
Maire, E., Withers, P.J., 2014. Quantitative X-ray tomography. Int. Mater. Rev. 59, 1–43.
Maji, A.K., Tasdemir, M.A., Shah, S.P., 1991. Mixed mode crack propagation in quasi-brittle materials. Eng. Fract. Mech. 38, 129–145.
Manouchehrian, A., Sharifzadeh, M., Marji, M.F., Gholamnejad, J., 2014. A bonded particle model for analysis of the flaw orientation effect on crack propagation mechanism in brittle materials under compression. Arch. Civ. Mech. Eng. 14, 40–52.
Martin, C.D., Chandler, N.A., 1994. The progressive fracture of Lac du Bonnet granite. Int. J. Rock Mech. Min. Sci. 31, 643–659.
Martin, C.D., 1997. Seventeenth Canadian geotechnical colloquium: the effect of cohesion loss and stress path on brittle rock strength. Can. Geotech. J. 34, 698–725.
Miao, S., Pan, P.Z., Wu, Z., Li, S., Zhao, S., 2018. Fracture analysis of sandstone with a single filled flaw under uniaxial compression. Eng. Fract. Mech. 204, 319–343.
Mitchell, T.M., Faulkner, D.R., 2009. The nature and origin of off-fault damage surrounding strike-slip fault zones with a wide range of displacements: a field study from the Atacama fault system, northern Chile. J. Struct. Geol. 31, 802–816.
Modiriasari, A., Bobet, A., Pyrak-Nolte, L.J., 2017. Active seismic monitoring of crack initiation, propagation, and coalescence in rock. Rock Mech. Rock Eng. 50, 2311–2325.
Modiriasari, A., Bobet, A., Pyrak-Nolte, L.J., 2020. Seismic wave conversion caused by shear crack initiation and growth. Rock Mech. Rock Eng. 53, 2805–2818.
Moradian, Z., Einstein, H.H., Ballivy, G., 2016. Detection of cracking levels in brittle rocks by parametric analysis of the acoustic emission signals. Rock Mech. Rock Eng. 49, 785–800.
Morgan, S.P., Johnson, C.A., Einstein, H.H., 2013. Cracking processes in Barre granite: fracture process zones and crack coalescence. Int. J. Fract. 180, 177–204.
Morgan, S.P., Einstein, H.H., 2017. Cracking processes affected by bedding planes in Opalinus shale with flaw pairs. Eng. Fract. Mech. 176, 213–234.
Morgan, S.P., Li, B.Q., Einstein, H.H., 2017. Effect of injection rate on hydraulic fracturing of Opalinus clay shale. In: 51st US Rock Mech./Geomech. Symp. 2017, 5, pp. 3085–3092.
Naderloo, M., Moosavi, M., Ahmadi, M., 2019. Using acoustic emission technique to monitor damage progress around joints in brittle materials. Theor. Appl. Fract. Mech. 104, 102368.
Nasseri, M.H.B., Schubnel, A., Young, R.P., 2007. Coupled evolutions of fracture toughness and elastic wave velocities at high crack density in thermally treated Westerly granite. Int. J. Rock Mech. Min. Sci. 44, 601–616.
Nemat-Nasser, S., Horii, H., 1982. Compression-induced nonplanar crack extension with application to splitting, exfoliation, and rockburst. J. Geophys. Res. 87, 6805–6821.
Nevitt, J.M., Pollard, D.D., Warren, J.M., 2014. Evaluation of transtension and transpression within contractional fault steps: comparing kinematic and mechanical models to field data. J. Struct. Geol. 60, 55–69.
Nevitt, J.M., Warren, J.M., Pollard, D.D., 2017. Testing constitutive equations for brittle-ductile deformation associated with faulting in granitic rock. J. Geophys. Res. Solid Earth 122, 6269–6293.
Nicksiar, M., Martin, C.D., 2012. Evaluation of methods for determining crack initiation in compression tests on low-porosity rocks. Rock Mech. Rock Eng. 45, 607–617.
Niu, Y., Zhou, X.P., Zhou, L.S., 2020. Fracture damage prediction in fissured red sandstone under uniaxial compression: acoustic emission b-value analysis. Fatig. Fract. Eng. Mater. Struct. 43, 175–190.
Ohno, K., Ohtsu, M., 2010. Crack classification in concrete based on acoustic emission. Construct. Build. Mater. 24, 2339–2346.
Pan, B., Qian, K., Xie, H., Asundi, A., 2009. Two-dimensional digital image correlation for in-plane displacement and strain measurement: a review. Meas. Sci. Technol. 20, 062001.
Pan, B., Xie, H., Wang, Z., 2010. Equivalence of digital image correlation criteria for pattern matching. Appl. Opt. 49, 5501–5509.
Pan, P.Z., Miao, S., Jiang, Q., Wu, Z., Shao, C., 2020. The influence of infilling conditions on flaw surface relative displacement induced cracking behavior in hard rock. Rock Mech. Rock Eng. 53, 4449–4470.
Park, C.H., 2008. Coalescence of Frictional Fractures in Rock Materials. PhD Thesis. Purdue University.
Park, C.H., Bobet, A., 2009. Crack coalescence in specimens with open and closed flaws: a comparison. Int. J. Rock Mech. Min. Sci. 46, 819–829.
Park, C.H., Bobet, A., 2010. Crack initiation, propagation and coalescence from frictional flaws in uniaxial compression. Eng. Fract. Mech. 77, 2727–2748.
Patil, P., Vyasarayani, C.P., Ramji, M., 2017. Linear least squares approach for evaluating crack tip fracture parameters using isochromatic and isoclinic data from digital photoelasticity. Opt Laser. Eng. 93, 182–194.
Peng, K., Wang, Y., Zou, Q., Liu, Z., Mou, J., 2019. Effect of crack angles on energy characteristics of sandstones under a complex stress path. Eng. Fract. Mech. 218, 106577.
Petrucci, G., 1997. Full-field automatic evaluation of an isoclinic parameter in white light. Exp. Mech. 37, 420–426.
Prudencio, M., Van Sint Jan, M., 2007. Strength and failure modes of rock mass models with non-persistent joints. Int. J. Rock Mech. Min. Sci. 44, 890–902.
Pu, C., Cao, P., 2012. Failure characteristics and its influencing factors of rock-like material with multi-fissures under uniaxial compression. Trans. Nonferrous Metals Soc. China 22, 185–191.
Qiu, S.L., Feng, X.T., Xiao, J.Q., Zhang, C.Q., 2014. An experimental study on the pre-peak unloading damage evolution of marble. Rock Mech. Rock Eng. 47, 401–419.
Ramesh, K., Ramakrishnan, V., 2016. Digital photoelasticity of glass: a comprehensive review. Opt Laser. Eng. 87, 59–74.
Ramesh, K., Sasikumar, S., 2020. Digital photoelasticity: recent developments and diverse applications. Opt Laser. Eng. 135, 106186.
Reyes, O., Einstein, H.H., 1991. Failure mechanisms of fractured rock - a fracture coalescence model. In: 7th ISRM Congress. International Society for Rock Mechanics and Rock Engineering, pp. 333–340.
Sagong, M., 2001. The Study on the Fracture of Multiple Flaw Specimens. PhD Thesis. Purdue University.
Sagong, M., Bobet, A., 2002. Coalescence of multiple flaws in a rock-model material in uniaxial compression. Int. J. Rock Mech. Min. Sci. 39, 229–241.
Sarfarazi, V., Haeri, H., 2016. A review of experimental and numerical investigations about crack propagation. Comput. Concr. 18, 235–266.
Sarma, A.V.S.S.S.R., Pillai, S.A., Subramanian, G., Varadan, T.K., 1992. Computerized image processing for whole-field determination of isoclinics and isochromatics. Exp. Mech. 32, 24–29.
Savitski, A.A., Detournay, E., 2002. Propagation of a penny-shaped fluid-driven fracture in an impermeable rock: asymptotic solutions. Int. J. Solid Struct. 39, 6311–6337.
Shan, R. liang, Bai, Y., Ju, Y., et al., 2021. Study on the triaxial unloading creep mechanical properties and damage constitutive model of red sandstone containing a single ice-filled flaw. Rock Mech. Rock Eng. 54, 833–855.
Sharafisafa, M., Shen, L., Xu, Q., 2018. Characterisation of mechanical behaviour of 3D printed rock-like material with digital image correlation. Int. J. Rock Mech. Min. Sci. 112, 122–138.
Sharafisafa, M., Shen, L., Zheng, Y., Xiao, J., 2019. The effect of flaw filling material on the compressive behaviour of 3D printed rock-like discs. Int. J. Rock Mech. Min. Sci. 117, 105–117.
Shen, B., 1993. Mechanics of Fractures and Intervening Bridges in Hard Rocks. PhD Thesis. Engineering Geology, Royal Institute of Technology.
Shen, B., 1995. The mechanism of fracture coalescence in compression-experimental study and numerical simulation. Eng. Fract. Mech. 51, 73–85.
Shen, B., Stephansson, O., Einstein, H.H., Ghahreman, B., 1995. Coalescence of fractures under shear stresses in experiments. J. Geophys. Res. Solid Earth 100, 5975–5990.
Shi, G., Yang, X., Yu, H., Zhu, C., 2019. Acoustic emission characteristics of creep fracture evolution in double-fracture fine sandstone under uniaxial compression. Eng. Fract. Mech. 210, 13–28.
Shirole, D., Hedayat, A., Ghazanfari, E., Walton, G., 2020. Evaluation of an ultrasonic method for damage characterization of brittle rocks. Rock Mech. Rock Eng. 53, 2077–2094.
Shirole, D., Hedayat, A., Walton, G., 2021. Damage monitoring in rock specimens with pre-existing flaws by non-linear ultrasonic waves and digital image correlation. Int. J. Rock Mech. Min. Sci. 142, 104758.
Sirdesai, N.N., Mahanta, B., Ranjith, P.G., Singh, T.N., 2019. Effects of thermal treatment on physico-morphological properties of Indian fine-grained sandstone. Bull. Eng. Geol. Environ. 78, 883–897.
Soliman, M.Y., Daal, J., East, L., 2012. Fracturing unconventional formations to enhance productivity. J. Nat. Gas Sci. Eng. 8, 52–67.
Sufian, A., Russell, A.R., 2013. Microstructural pore changes and energy dissipation in Gosford sandstone during pre-failure loading using X-ray CT. Int. J. Rock Mech. Min. Sci. 57, 119–131.
Swain, D., Philip, J., Pillai, S.A., Ramesh, K., 2016. A revisit to the frozen stress phenomena in photoelasticity. Exp. Mech. 56, 903–917.
Tal, Y., Evans, B., Mok, U., 2016. Direct observations of damage during unconfined brittle failure of Carrara marble. J. Geophys. Res. Solid Earth 121, 1584–1609.
Tian, H., Mei, G., Jiang, G.S., Qin, Y., 2017. High-temperature influence on mechanical properties of diorite. Rock Mech. Rock Eng. 50, 1661–1666.
Tian, W.L., Yang, S.Q., Xie, L.X., Wang, Z.L., 2018. Cracking behavior of three types granite with different grain size containing two non-coplanar fissures under uniaxial compression. Arch. Civ. Mech. Eng. 18, 1580–1596.
Virgo, S., Abe, S., Urai, J.L., 2013. Extension fracture propagation in rocks with veins: insight into the crack-seal process using Discrete Element Method modeling. J. Geophys. Res. Solid Earth 118, 5236–5251.
Vivekanandan, A., Ramesh, K., 2019. Study of interaction effects of asymmetric cracks under biaxial loading using digital photoelasticity. Theor. Appl. Fract. Mech. 99, 104–117.
Wan, W., Liu, J., Zhao, Y., Fan, X., 2019. The effects of the rock bridge ligament angle and the confinement on crack coalescence in rock bridges: an experimental study and discrete element method. Compt. Rendus Mec. 347, 490–503.
Wang, R., Zhao, Yusheng, Chen, Yong, et al., 1987. Experiment and finite element simulation of X-type shear fractures from a crack in marble. Tectonophysics 144, 141–150.

Wang, J., 2010. High-level radioactive waste disposal in China: update 2010. J. Rock Mech. Geotech. Eng. 2, 1–11.
Wang, D.J., Tang, H., Elsworth, D., Wang, C., 2019a. Fracture evolution in artificial bedded rocks containing a structural flaw under uniaxial compression. Eng. Geol. 250, 130–141.
Wang, H., Dyskin, A., Pasternak, E., 2019b. Comparative analysis of mechanisms of 3-D brittle crack growth in compression. Eng. Fract. Mech. 220, 106656.
Wang, D.J., Tang, H., Shen, P., Su, X., Huang, L., 2020a. Co-effects of bedding planes and parallel flaws on fracture evolution in anisotropic rocks. Eng. Geol. 264, 105382.
Wang, M., Wan, W., Zhao, Y., 2020b. Experimental study on crack propagation and the coalescence of rock-like materials with two preexisting fissures under biaxial compression. Bull. Eng. Geol. Environ. 79, 3121–3144.
Wang, Y., Feng, W.K., Wang, H.J., Li, C.H., Hou, Z.Q., 2020c. Rock bridge fracturing characteristics in granite induced by freeze-thaw and uniaxial deformation revealed by AE monitoring and post-test CT scanning. Cold Reg. Sci. Technol. 177, 103115.
Wang, Y., Zhang, H., Lin, H., et al., 2020d. Mechanical behavior and failure analysis of fracture-filled gneissic granite. Theor. Appl. Fract. Mech. 108, 102674.
Wang, X., Wang, E., Liu, X., Zhou, X., 2021a. Failure mechanism of fractured rock and associated acoustic behaviors under different loading rates. Eng. Fract. Mech. 247, 107674.
Wang, Y., Gao, Y., Liu, Y., et al., 2021b. Optimal aperture and digital speckle optimization in digital image correlation. Exp. Mech. 61, 677–684.
Wijerathne, M.L.L., Oguni, K., Hori, M., 2008. Stress field tomography based on 3D photoelasticity. J. Mech. Phys. Solid. 56, 1065–1085.
Wong, R.H.C., Chau, K.T., 1998. Crack coalescence in a rock-like material containing two cracks. Int. J. Rock Mech. Min. Sci. 35, 147–164.
Wong, L.N.Y., Einstein, H., 2006. Fracturing behavior of prismatic specimens containing single flaws. In: Proceedings of the 41st U.S. Rock Mechanics Symposium - ARMA's Golden Rocks 2006 - 50 Years of Rock Mechanics.
Wong, R.H.C., Guo, Y.S.H., Li, L.Y., et al., 2006. Anti-wing crack growth from surface flaw in real rock under uniaxial compression. In: Fracture of Nano and Engineering Materials and Structures - Proceedings of the 16th European Conference of Fracture. Springer, Netherlands, Dordrecht, pp. 825–826.
Wong, N.Y., 2008. Crack Coalescence in Molded Gypsum and Carrara Marble. PhD Thesis. Massachusetts Institute of Technology.
Wong, L.N.Y., Einstein, H.H., 2009a. Crack coalescence in molded gypsum and carrara marble: Part 1. macroscopic observations and interpretation. Rock Mech. Rock Eng. 42, 475–511.
Wong, L.N.Y., Einstein, H.H., 2009b. Systematic evaluation of cracking behavior in specimens containing single flaws under uniaxial compression. Int. J. Rock Mech. Min. Sci. 46, 239–249.
Wong, L.N.Y., Li, H.Q., 2013. Numerical study on coalescence of two pre-existing coplanar flaws in rock. Int. J. Solid Struct. 50, 3685–3706.
Wong, L.N.Y., Xiong, Q., 2018. A method for multiscale interpretation of fracture processes in carrara marble specimen containing a single flaw under uniaxial compression. J. Geophys. Res. Solid Earth 123, 6459–6490.
Wu, H.C., Chang, K.J., 1978. Angled elliptic notch problem in compression and tension. J. Appl. Mech. Trans. ASME 45, 258–262.
Xing, H.Z., Zhang, Q.B., Ruan, D., et al., 2018. Full-field measurement and fracture characterisations of rocks under dynamic loads using high-speed three-dimensional digital image correlation. Int. J. Impact Eng. 113, 61–72.
Xue, L., Qin, S., Sun, Q., et al., 2014. A study on crack damage stress thresholds of different rock types based on uniaxial compression tests. Rock Mech. Rock Eng. 47, 1183–1195.
Yan, Z., Dai, F., Liu, Y., Du, H., Luo, J., 2020. Dynamic strength and cracking behaviors of single-flawed rock subjected to coupled static–dynamic compression. Rock Mech. Rock Eng. 53, 4289–4298.
Yan, Z., Dai, F., Liu, Y., Li, Y., You, W., 2021. Experimental investigation of pre-flawed rocks under combined static-dynamic loading: mechanical responses and fracturing characteristics. Int. J. Mech. Sci. 211, 106755.
Yang, S.Q., Jing, H.W., 2011. Strength failure and crack coalescence behavior of brittle sandstone samples containing a single fissure under uniaxial compression. Int. J. Fract. 168, 227–250.
Yang, S.Q., Liu, X.R., Jing, H.W., 2013. Experimental investigation on fracture coalescence behavior of red sandstone containing two unparallel fissures under uniaxial compression. Int. J. Rock Mech. Min. Sci. 63, 82–92.
Yang, S.Q., Jing, H.W., Huang, Y.H., Ranjith, P.G., Jiao, Y.Y., 2014. Fracture mechanical behavior of red sandstone containing a single fissure and two parallel fissures after exposure to different high temperature treatments. J. Struct. Geol. 69, 245–264.
Yang, S.Q., Tian, W.L., Huang, Y.H., Ranjith, P.G., Ju, Y., 2016. An experimental and numerical study on cracking behavior of brittle sandstone containing two non-coplanar fissures under uniaxial compression. Rock Mech. Rock Eng. 49, 1497–1515.
Yang, S.Q., Ranjith, P.G., Jing, H.W., Tian, W.L., Ju, Y., 2017a. An experimental investigation on thermal damage and failure mechanical behavior of granite after exposure to different high temperature treatments. Geothermics 65, 180–197.
Yang, X.X., Jing, H.W., Tang, C.A., Yang, S.Q., 2017b. Effect of parallel joint interaction on mechanical behavior of jointed rock mass models. Int. J. Rock Mech. Min. Sci. 92, 40–53.
Yang, S.Q., Huang, Y.H., Tian, W.L., Yin, P.F., Jing, H.W., 2019. Effect of high temperature on deformation failure behavior of granite specimen containing a single fissure under uniaxial compression. Rock Mech. Rock Eng. 52, 2087–2107.
Yin, P., Wong, R.H.C., Chau, K.T., 2014. Coalescence of two parallel pre-existing surface cracks in granite. Int. J. Rock Mech. Min. Sci. 68, 66–84.
Yuan, Y., Pan, P., Zhao, S., Wang, B., Song, G., 2018. The failure process of marble with filled crack under uniaxial compression based on digital image correlation. Yanshilixue Yu Gongcheng Xuebao/Chinese J. Rock Mech. Eng. 37, 339–351.
Zhang, X.P., Wong, L.N.Y., 2012. Cracking processes in rock-like material containing a single flaw under uniaxial compression: a numerical study based on parallel bonded-particle model approach. Rock Mech. Rock Eng. 45, 711–737.
Zhang, G.K., Li, H.B., Wang, M.Y., Li, X.F., 2020. Crack initiation of granite under uniaxial compression tests: a comparison study. J. Rock Mech. Geotech. Eng. 12, 656–666.
Zhao, Y., 2004. Mini-crack development from a cemented fracture in marble specimen under uniaxial compression. Yanshilixue Yu Gongcheng Xuebao/Chinese J. Rock Mech. Eng. 23, 2504–2509.
Zhao, Y.H., Yang, Z.T., 2005. Research on fracturing around cemented slot in rock specimen. Yanshilixue Yu Gongcheng Xuebao/Chinese J. Rock Mech. Eng. 24, 2350–2356.
Zhao, Z., Zhou, D., 2016. Mechanical properties and failure modes of rock samples with grout-infilled flaws: a particle mechanics modeling. J. Nat. Gas Sci. Eng. 34, 702–715.
Zhao, Y., Zhang, L., Wang, W., et al., 2016. Cracking and stress–strain behavior of rock-like material containing two flaws under uniaxial compression. Rock Mech. Rock Eng. 49, 2665–2687.
Zhao, C., Zhou, Y. meng, Zhao, C. feng, Bao, C., 2018. Cracking processes and coalescence modes in rock-like specimens with two parallel pre-existing cracks. Rock Mech. Rock Eng. 51, 3377–3393.
Zhao, C., Niu, J., Zhang, Q., Zhao, C., Zhou, Y., 2019. Failure characteristics of rock-like materials with single flaws under uniaxial compression. Bull. Eng. Geol. Environ. 78, 593–603.
Zhao, C., Xing, J., Zhou, Y., Shi, Z., Wang, G., 2020. Experimental investigation on hydraulic fracturing of granite specimens with double flaws based on. DIC. Eng. Geol. 267, 105510.
Zhou, X.P., Cheng, H., Feng, Y.F., 2014. An experimental study of crack coalescence behaviour in rock-like materials containing multiple flaws under uniaxial compression. Rock Mech. Rock Eng. 47, 1961–1986.
Zhou, X.P., Lian, Y.J., Wong, L.N.Y., Berto, F., 2018. Understanding the fracture behavior of brittle and ductile multi-flawed rocks by uniaxial loading by digital image correlation. Eng. Fract. Mech. 199, 438–460.
Zhou, X.P., Niu, Y., Zhang, J.Z., et al., 2019a. Experimental study on effects of freeze-thaw fatigue damage on the cracking behaviors of sandstone containing two unparallel fissures. Fatig. Fract. Eng. Mater. Struct. 42, 1322–1340.
Zhou, X.P., Zhang, J.Z., Qian, Q.H., Niu, Y., 2019b. Experimental investigation of progressive cracking processes in granite under uniaxial loading using digital imaging and AE techniques. J. Struct. Geol. 126, 129–145.
Zhou, X., Niu, Y., Cheng, H., Berto, F., 2021a. Cracking behaviors and chaotic characteristics of sandstone with unfilled and filled dentate flaw. Theor. Appl. Fract. Mech. 112, 102876.
Zhou, X.P., Zhang, J.Z., Yang, S.Q., Berto, F., 2021b. Compression-induced crack initiation and growth in flawed rocks: a review. Fatig. Fract. Eng. Mater. Struct. 44, 1681–1707.
Zhu, T., Jing, H., Su, H., et al., 2016. Physical and mechanical properties of sandstone containing a single fissure after exposure to high temperatures. Int. J. Min. Sci. Technol. 26, 319–325.
Zhuang, X., Chun, J., Zhu, H., 2014. A comparative study on unfilled and filled crack propagation for rock-like brittle material. Theor. Appl. Fract. Mech. 72, 110–120.

Prof. Haibo Li received his BSc degree from Zhengzhou Institute of Technology (i.e. Zhengzhou University since 2000), Zhengzhou, China in 1992. He received his PhD from Institute of Rock and Soil Mechanics (IRSM), Chinese Academy of Sciences, Wuhan, China in 1999. During 1998–2000, he was a research assistant in School of Civil and Environmental Engineering, Nanyang Technological University, Singapore. Since 1997, he worked at IRSM as an assistant professor, associate professor, and professor. His research interests focus on rock dynamics and earthquake engineering, aiming to reveal the underlying failure mechanisms of rock or rock mass under dynamic loadings. To date, he is a member of Editorial Board of *International Journal of Rock Mechanics and Mining Sciences*, *Chinese Journal of Rock Mechanics and Engineering*, *Rock and Soil Mechanics*, etc. He is also a vice Editor-in-Chief of *Journal of Rock Mechanics and Geotechnical Engineering*.